A STUDY OF SUMMER LEESIDE RAINFALL OVER THE ISLANDS OF HAWAI'I AND OAHU

A THESIS SUBMITTED TO THE GRADUATE DIVISION OF THE UNIVERSITY OF HAWAI'I MĀNOA IN PARTIAL FULFILLMENT OF THE REQUIREMENTS FOR THE DEGREE OF

MASTER OF SCIENCE

IN

ATMOSPHERIC SCIENCES

MAY 2016

By

Yu-Fen Huang

Thesis Committee:

Yi-Leng Chen, Chairperson
Gary Barnes
Michael Bell

ACKNOWLEDGMENTS

I would first like to thank my advisor, Dr. Yi-Leng Chen, for his guidance, support, and patience through my entire master program. I want to thank Dr. Gary Barnes and Dr. Michael Bell for editing, reviewing, and motivating that recharged me and kept my research to the right direction. I appreciate Gary Grunseich for the help in English writing. I would also like to extend my gratitude to Feng Hsiao and Jie Chen for discussions, suggestions, and supports during this process. I also appreciate Wai Leung Lee, Francis Mai, Michael Gonsalves, Xiao Cheng, and all the colleagues for supports and giving me a good environment to work on my thesis. This process is supported by National Science Foundation. In the end, I really want to thank my parents and all of my family-like friends for their encouragement and supports to finish my program.

ABSTRACT

The Kona side of the island of Hawai'i is the only leeside of the Hawaiian Islands that exhibits pronounced summer rainfall maxima. In contrast, there is no marked rainfall maximum on the west coast of Oahu. In order to diagnose the physical processes for the rainfall in the Kona area and western Oahu, the historical daily real-time experimental forecasts for both the annual and diurnal cycles were analyzed using the fifth-generation Pennsylvania State University-NCAR Mesoscale Model (MM5) coupled with the advanced land surface model (LSM) from June 2004 to February 2010.

During the summer trade-wind days, trades (6-8 m s^{-1}) are persistent with significant orographic blocking over the Island of Hawai'i. A relatively strong and moist westerly reversed flow appears adjacent to the Kona coast. The flow over Hawai'i is under a low (~0.3) Froude-number (Fr)-flow regime for the massive mountains, which are well above the trade wind inversion (TWI). Furthermore, the diurnal heating cycle on Hawai'i is strongest in summer. Enhanced orographic lifting due to both westerly reversed flow and the upslope flow, combined with higher moisture content, one of summer rainfall maxima occurs in the afternoon hours on the lower Kona slopes. In addition, a nocturnal rainfall maximum occurs just west of the Kona coast due to convergence between offshore flow and the westerly reversed flow. During the summer, the westerly reversed flow is stronger with higher moisture content than during the

winter. Therefore, the nocturnal rainfall offshore of Kona also has a summer maximum.

In contrast, the Ko’olau and the Waianae mountains of Oahu are below the TWI with Fr ~ 1. Thus, the airflow aloft can cross the mountains and descend on the leeside of both mountain ranges. For the west leeside of Oahu, the air is warmer and drier than on the windward side due to the rain shadow effect, daytime heating and vertical mixing. Therefore, afternoon showers are infrequent on the west leeside of Oahu during the summer trade-wind days. During the night, the descending airflow on the west leeside is followed by a hydraulic jump without a westerly reversed flow, and there is no nocturnal rainfall maximum adjacent to the western coast of Oahu.

TABLE OF CONTENTS

LIST OF FIGURES

Figure Page

CHAPTER 1

Introduction

1.1 Background

The Hawaiian Islands are located in the trade wind belt. The trade wind showers are frequent due to interactions of trade wind flow with terrain (Leopold 1949; Garrett 1980; Schroeder 1981; Giambelluca et al. 1986; Chen and Nash 1994). Climatologically, northeasterly trade winds of 5 to 10 m s^{-1} are persistent throughout the year, especially during the summer months when the maximum trade wind occurrence reaches 92% in August. In winter, the trade wind occurrence is has a frequency lower than 50% in January (Schroeder 1993).

Most of the areas in the Hawaiian Islands exhibit a rainfall maximum during the cool season (October to April), and the rainfall is mainly related to the synoptic-scale disturbances — cold fronts, Kona lows, and upper-level troughs (Blumenstock and Price 1967) and their interaction with terrain and local winds. However, the Kona area on the island of Hawai'i is the only region in the state that has a summer rainfall maximum (Meisner 1976; Giambelluca et al. 1986, 2013). A comparison of annual and diurnal leeside circulations between summer and winter, and a study of the winter trade-wind days will improve our understanding of why the leeside rainfall maximum over Hawai'i occurs in summer.

Leopold (1949) suggested that the spatial distribution of rainfall over the Hawaiian Islands is related to orographic effects, the height of the trade wind inversion, and thermally driven diurnal winds. The blocking effect occurs when the airflow passes a three-dimensional obstacle under a low (< 1) Froude number (Fr)-flow regime (Fr = $\boldsymbol{U}/\mathrm{N}h$, where $\boldsymbol{U}$ is the upstream wind speed, N is the Brunt–Väisälä frequency, and h is the height of the barrier). In addition to Fr, the TWI (~ 2 km over the Hawaiian Islands) serves as a lid, forcing the low-level flow to go around the mountains with tops higher than the TWI (Leopold 1949). With different mountain heights, the summer leeside rainfall will be compared between Hawai'i and Oahu to diagnose the physical processes responsible for the leeside of Hawai'i exhibiting a summer rainfall maximum.

1.2 Previous studies on the island of Hawai'i

The island of Hawai'i is the largest island in the Hawaiian Islands, dominated by two massive volcanic mountains, Mauna Loa and Mauna Kea, both exceeding 4,100 m in height, much higher than the typical height of the TWI. Considering a well-mixed trade-wind layer decoupled by TWI, an average value of Fr is about 0.5 (Smith and Grubišić 1993). The large wake adjacent to the Kona coast with two large counter-rotating vortices (Patzert 1969; Nickerson and Dias 1981; Smith and Grubišić 1993) is caused by orographic blocking under a low Fr-flow regime and the presence of the TWI.

By using the 50 surface data collected during the Hawaiian Rainband Project (HaRP; 11 July – 24 August 1990), Chen and Nash (1994) showed that the surface airflow and rainfall occurrences are strongly modulated by the diurnal heating cycle over Hawai'i. Furthermore, in the regions with weak trade winds because of island blocking, the diurnal land-sea breezes with upslope/onshore flow during the day and downslope/offshore flow at night become significant (Schroeder et al. 1977; Feng and Chen 1998; Chen and Nash 1994).

On the leeside of Hawai'i, Leopold (1949) suggested that the summer showers in the Kona area in the afternoon are related to sea breezes, which brought the convective clouds inland. In the evening, the daily rainfall maximum occurs along the Kona coast because of the convergence between the westerly reversed flow and the offshore/katabatic flow (Yang et al. 2003; Yang et al.

2008). Under strong trade-wind conditions (~7.9 m s^{-1}), the evening rainfall in the Kona coastal region is greater than in weak trade wind cases (~5.2 m s^{-1}) because the westerly reversed flow is stronger when the trade wind speeds are higher (Yang et al. 2008).

1.3 Previous studies over Oahu

In contrast to the island of Hawai'i, the mountains over Oahu are well below the TWI. The Ko'olau Mountains (~ 960 m) extend about 45 km along Oahu's eastern coast, and the Waianae Mountains (~ 1,200 m) extend about 30 km along the western coast of Oahu. Nguyen et al. (2010) showed that $U/N \sim h$ under summer trade-wind conditions, and low-level air parcels can cross the Ko'olau Mountains. In addition to the lower terrain heights, the island sizes is another factor that influences rainfall (Yang and Chen; 2008).

Because of orographic lifting, the horizontal distribution of rainfall shows a maximum over the Ko'olau Mountains with a secondary rainfall maximum over the Waianae Mountains (Hartley and Chen 2010). Winds over the island interior are weaker than over the open ocean because of orographic blocking and land surface friction. Furthermore, some of the moisture are removed by orographic precipitation over the Ko'olau Mountains, and it causes drier conditions downstream. Thus, rainfall on the leeside of the Ko'olau and the Waianae mountains is much less than the windward side of Oahu. Over the Ko'olau Mountains a nocturnal rainfall maximum occurs in the early morning, possibly due to cloud top radiation cooling (Leopold 1949) with significant flow deceleration at the surface on the windward side when the land surface is the coldest (Nguyen et al. 2010). Furthermore, the level of free convection (LFC) is the lowest in the early morning. A secondary diurnal rainfall maximum occurs along the leeward slope of the Waianae Mountains after sunset, most likely related to more significant orographic lifting (Nguyen et al. 2010). In addition to the speed of the incoming trade winds, the trade wind orographic rainfall is affected by the moisture content of the incoming flow and the height of the TWI (Hartley and Chen 2010). According to Hartley and Chen (2010), trade wind orographic rainfall amount tends to be greater when the TWI is higher.

At night, when the westerly mountain winds on the eastern slopes of the Waianae Mountain Range are present, the winds are calm over central Oahu between the Ko'olau Mountains and the Waianae Mountains. The thermally diurnal driven winds are more pronounced on the leeside than on the windward side of Oahu (Hartley and Chen 2010). On the west leeside coast, trade wind showers are infrequent. The afternoon sea breezes may increase the chance for cloud development on the western coast of Oahu, especially under weak trade conditions (Hartley and Chen 2010; Nguyen et al. 2010).

1.4 Objectives

The airflows over the island of Hawai'i and Oahu are well studied from both observations and simulations using the MM5/LSM model. The previous studies have focused on simulated airflow and rainfall over the islands during HaRP (Yang et al. 2005) and two summer months in 2005 (Yang et al. 2008; Nguyen et al. 2010). In this study, the 6-yr-archive of daily MM5/LSM data (June 2004 and February 2010) will be used to answer the following questions:

- What are the differences in leeside rainfall maxima between summer and winter for the island of Hawai'i?
- What are the differences in the diurnal variations of rainfall on the leeside slope and offshore flow over Hawai'i?

- What are the mean differences on the leeside of Hawai'i between the entire winter season and the winter trade-wind days?
- What are the differences in leeside rainfall during the summer months between Hawai'i and Oahu?

CHAPTER 2

Data and Method

2.1 Data

A high-resolution simulation is needed since the global model output from the National Centers for Environmental Prediction (NCEP) is too coarse to resolve the local weather and circulations with the complex island terrain over the Hawai'i Islands. The nonhydrostatic Mesoscale Model version 5 (MM5) is a three-dimensional primitive equation model with the terrain-following sigma vertical coordinate. The MM5 coupled with the advanced land surface model (LSM) employs soil moisture and temperature with four layers at depths of 10, 40, 100, and 200 cm (Chen and Dudhia 2001). The land use, soil type, and vegetation cover for the islands of Hawai'i and Oahu employed in the model were compiled by Zhang et al. (2005a).

The daily MM5-LSM experimental simulations had been conducted during June 2004 – February 2010 for the islands of Hawai'i and Oahu with soil moisture and soil temperature updated from the 24-hr forecast of the previous day. The daily 36-hr MM5 runs were initialized by the NCEP Global Forecast System (GFS) data at 0000 UTC, and the sea surface temperature (SST) is from the NCEP SST analysis. The simulated diurnal cycles are represented by the model daily output during the 12^{th} - 35^{th} hour simulation.

For the island of Hawai'i, Yang et al. (2005) successfully simulated the island-scale circulation and rainfall during the diurnal cycle by using MM5/LSM. Their simulations were validated with the HaRP data, including data from 50 surface stations, Hilo soundings, as well as aircraft flight-level data (Yang et al. 2005; Yang and Chen 2008; Yang et al. 2008). The simulations of surface airflow, temperature, moisture, and rainfall and their diurnal variations during July - August 2005 over Oahu were validated by 13 hourly weather stations and 69 rain gauge stations (Nguyen et al. 2010).

In this study, four nested domains with two-way nesting were employed to simulate the leeside circulations over the islands of Hawai'i and Oahu. There are 29[1] sigma levels from the surface to the 100-hPa level, and similarity theory is used for profiles in the surface layer. The horizontal grid sizes are 81, 27, 9, and 3 km (Fig. 1a) over Hawai'i (Yang et al. 2005; Yang et al. 2008), and 40.5, 13.5, 4.5, and 1.5 km (Fig. 1b) over Oahu (Nguyen et al. 2010), respectively.

The physic options are the same for both the islands of Hawai'i (Yang et al. 2005; Yang et al. 2008) and Oahu (Nguyen et al. 2010). Grell's cumulus parameterization (Grell 1993), an explicit grid-scale warm rain microphysics (Hsie et al. 1984), a cloud radiation scheme (Dudhia and Moncrieff 1989), and the medium-range forecast (MRF) planetary boundary layer scheme (Hong and Pan 1996) are used in the model. Grell's cumulus parameterization, which is based on the rate of destabilization or quasi-equilibrium, includes a simple single-cloud scheme with updraft and downdraft fluxes and compensating motion determining the heating/moistening profile (Grell 1993). The cumulus parameterization scheme is not used for the 1.5-km Oahu and 3-km Hawai'i domains. The grid-scale warm rain microphysics predicts explicitly with microphysical processes without ice-phase processes (Hsie et al. 1984). The Duhia radiation scheme (Dudhia 1989) can account for longwave and shortwave interactions with explicit clouds and clear air; moreover, it provides surface radiation fluxes.

2.2 The trade-wind days

The trade-wind days in winter are selected by using the NCEP/FNL re-analysis data. The trade-wind days are the days with upstream wind direction between 45˚ to 100˚, but without

[1] The full sigma levels are 1.0, 0.998, 0.994, 0.990, 0.985, 0.980, 0.970, 0.945, 0.91, 0.865, 0.82, 0.79, 0.76, 0.72, 0.68, 0.63, 0.58, 0.52, 0.475, 0.425, 0.375, 0.325, 0.275, 0.225, 0.175, 0.125, 0.075, 0.025, and 0.0.

a tropical cyclone, Kona low, cold front, or an upper-level trough at the 250-hPa level within 170˚W to 145˚W and 12˚N to 28˚N. The post-frontals days and thunderstorm days with strong easterly winds are also removed. The occurrences of trade-wind days from June 2004 to February 2010 are 77% in the summer months (June, July, and August) and 26.1% in the winter months (December, January, and February), respectively.

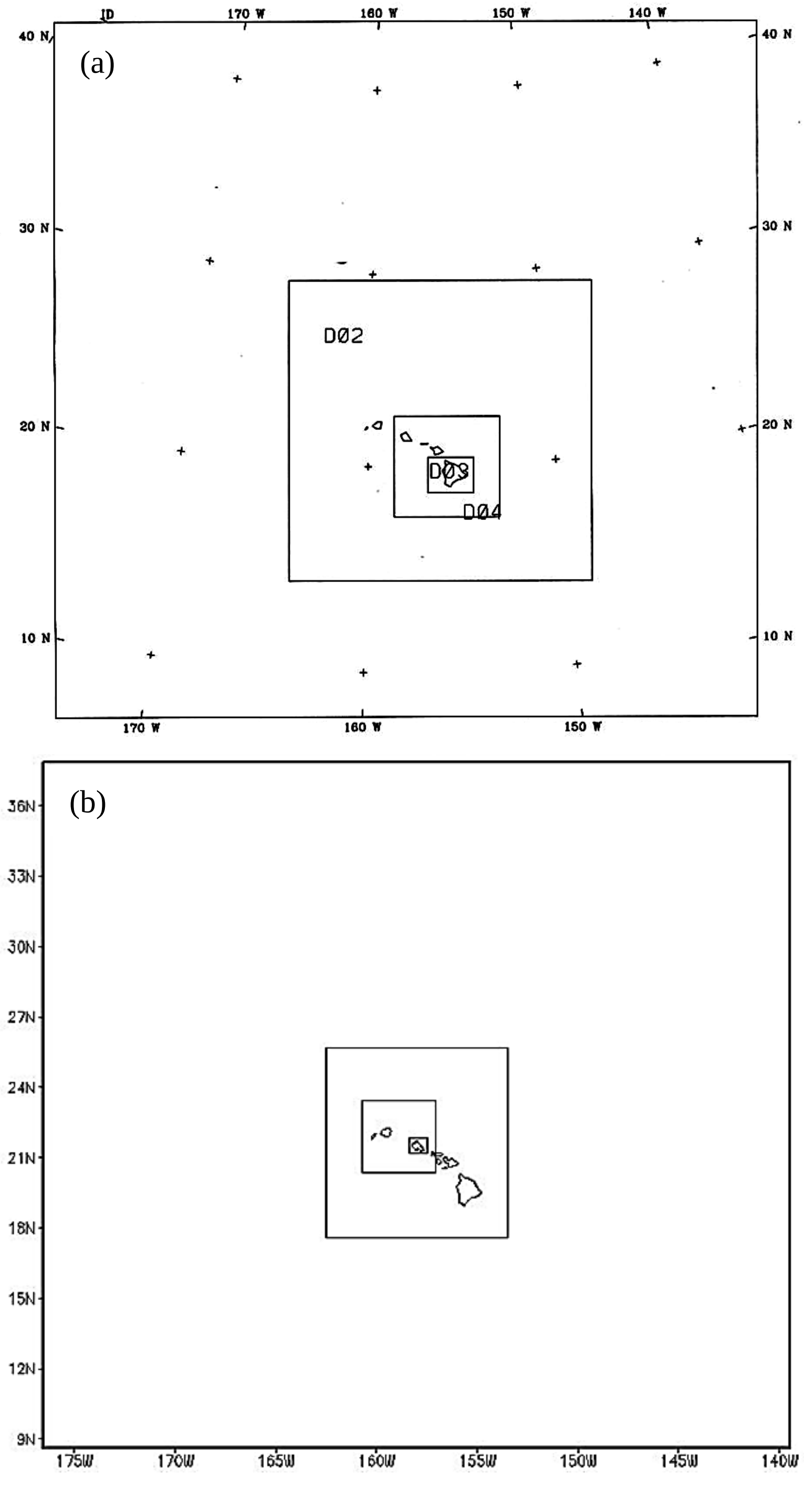

Fig. 1 (a) The four nested domains with resolution of 81, 27, 9, and 3 km over the island of Hawai'i. (Yang et al. 2008); (b) The four nested domains with resolution of 40.5, 13.5, 4.5, and 1.5 km over Oahu. (Nguyen et al. 2010)

CHAPTER 3

A Comparison of Simulated Leeside Circulations between Summer and Winter over the Island of Hawai'i

In this chapter, I will answer what the reasons for more leeside rainfall over the island of Hawai'i during the summer months than during the winter months are. The differences in simulated rainfall, winds, and thermodynamic variables between summer (June, July, and August) and winter (December, January, and February) will be compared. Since the rainfall on the Kona leeside over the Hawai'i in summer is similar as under summer trade-wind days, and for the comparison between summer and winter under the trade-wind conditions next chapter, the figures of summer trade-wind days are shown here. All the figures for the entire summer months are in appendix for reference.

3.1 Simulated Mean State

a) Winds

For the summer trade-wind days, the simulated mean incoming winds from the northeast are > 6 m s^{-1} over the ocean (Fig. 2a), and the winds weaken to 2.5 m s^{-1}, and are deflected before they arrive at the windward coast due to orographic blocking. The wind speeds (Fig. 2a) are > 8.5 m s^{-1} and > 10 m s^{-1} at the southern and northern tips of the island, respectively. They are stronger within the 'Alenuihāhā Channel between the islands of Hawai'i and Maui than the southern tip because of the along-gap pressure gradients with lower pressure in the wakes of both islands (Hitzl et al. 2014). On the leeside, the trade winds (Fig. 2a) are completely blocked by the mountains and TWI with a low Fr (~ 0.3). The maximum westerly reversed wind between the counter-rotating vortices just west of the Kona coast is about 2.5 m s^{-1} for the large wake.

The simulated daily mean 10-m winds during the winter months from 2004 to 2010 (Fig. 2b) show that the incoming easterly winds (> 4.5 m s^{-1}) are about 1.5 m s^{-1} weaker than during the summer trade-wind days (Fig. 2a). The mean winds for the winter months (Fig. 2b) at both the northern (~ 6.5 m s^{-1}) and the southern (~ 7 m s^{-1}) tips are much weaker than during the summer trade-wind days. On the leeside of the island, the mean westerly reversed flow between the counter-rotating vortices during the winter months (~ 1 m s^{-1}) (Fig. 2b) is about 1.5 m s^{-1} weaker than during the summer trade-wind days (Fig. 2a) since the weaker incoming wind in winter.

b) Thermodynamic variables

The simulated mean 2-m air temperatures over land during the summer trade-wind days are about 2 to 4 ℃ higher than during the winter months (Fig. 2c). Over the ocean, the simulated mean 2-m air temperatures are about 1.5 to 2 ℃ greater than during the winter months (Fig. 2c). For the summer trade-wind days, the simulated minimum air temperature (24℃) over the ocean adjoining west of the leeside of the island is related to cloud cover and perhaps evaporative cooling, which is consistent with the summer leeside rainfall maximum there (Fig. 3a).

During the summer trade-wind days, the simulated mean total precipitable water (TPW) over the ocean on the windward side is 4.5 mm higher than during the winter months (Fig. 2d). Moreover, the TPW maximum adjacent to the Kona coast under the summer trade-wind conditions is much higher (> 7.5 mm) than during the winter months (Fig. 2d).

c) Precipitation

The overall simulated rainfall pattern during summer is remarkably similar to the total rainfall accumulation during HaRP (Chen and Nash 1994; Chen and Feng 1995). The simulated rainfall on the windward side is lower than climatological rainfall reported by Giambelluca et al. (1986, 2013), which may be considered in this study while the rainfall on the windward side and on the leeside are dependent to each other. Nevertheless, the simulated rainfall in the Kona area is consistent with the climatological observation (Giambelluca et al. 1986, 2013).

The simulated 6-year mean daily rainfalls over Hawai'i for both summer and winter exhibit a rainfall maximum on the windward lowlands near Hilo (Fig. 3) due to orographic lifting. The mean daily rainfall on the windward side is about 2 mm higher during the winter months (Fig. 3b) than during the summer trade-wind days (Fig. 3a) because of the frequently synoptic disturbances in winter. The other daily rainfall maximum for both seasons is found over northeastern Hawai'i on the windward side of the Kohala Mountains (Fig. 3). Figure 3 also shows that the driest areas in both seasons are found on the summits of Mauna Loa and Mauna Kea, as well as northwestern Hawai'i downstream of the Waimea Saddle. Relatively little rainfall is also found along the southeastern coast on the leeside of the Kilauea volcanoes and the southwestern coast behind the southern ridge axis of Mauna Loa caused by rain shadow effect. Over the central Kona region, there are two significant daily rainfall maxima (6 mm each) on the lowlands and offshore during the summer trade-wind days (Fig. 3a) but are not evident in the same areas during the winter months (Fig. 3b). It is apparent that the leeside rainfall maxima are not of synoptic origin. During the summer trade-wind days, the westerly reversed flow adjacent to the Kona leeside coast is stronger with a higher moisture content than during the winter months (Fig. 2). It appears that higher rainfall near central Kona during the summer trade-wind days (Fig. 3a) than the winter months (Fig. 3b) may be related to interactions between the moist westerly flow, the diurnally driven local winds and terrain in the region, and will be further discussed in section 3.2.

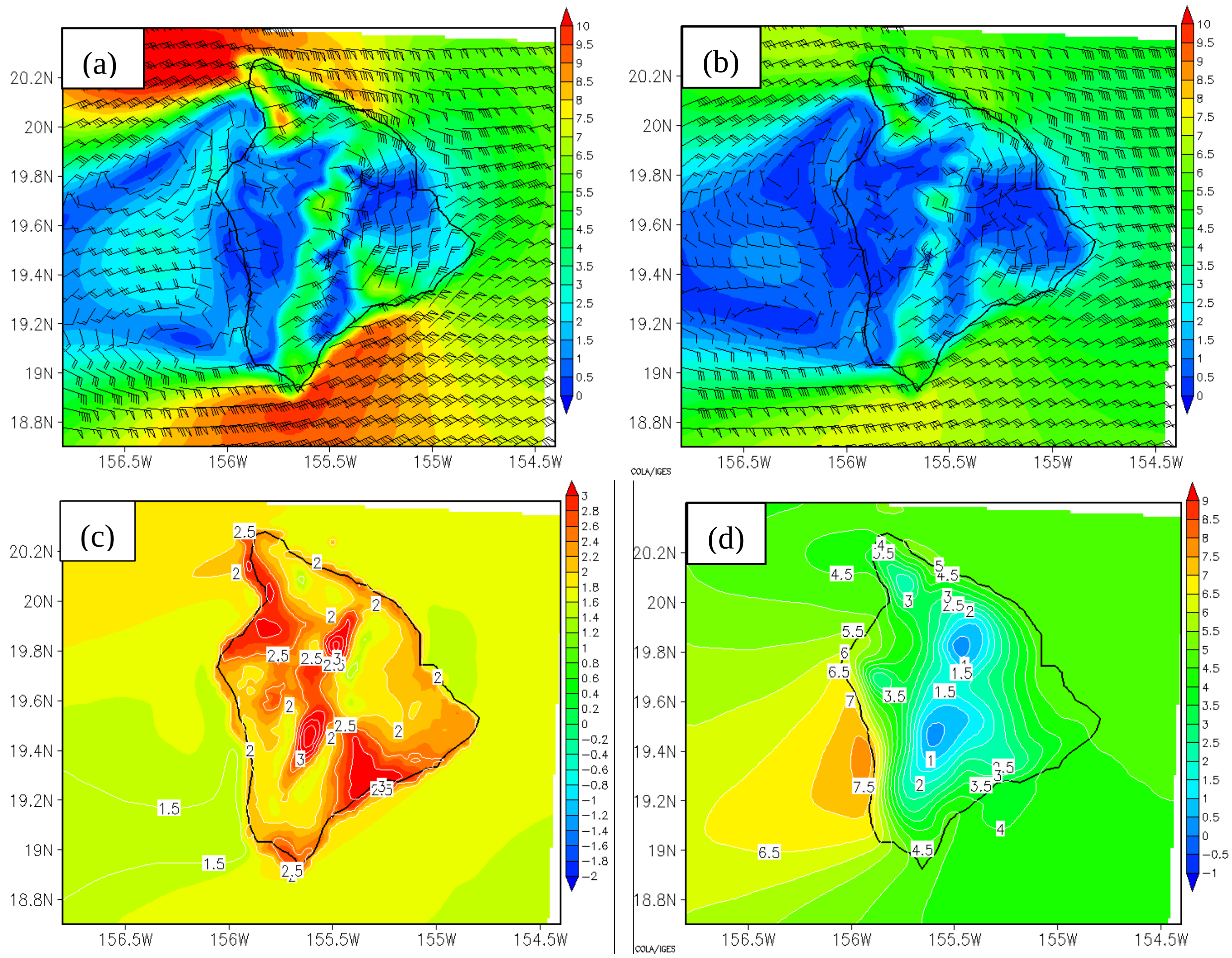

Fig. 2　The MM5/LSM simulated mean 10-m wind (m s^{-1}; full barb: 1 m s^{-1}, pennant: 5 m s^{-1}) (a) during the summer trade-wind days, (b) during the winter months.　The simulated (c) temperature differences (summer trade-wind days minus winter; ℃), and (d) mean total precipitable water difference (mm) over Hawai’i.

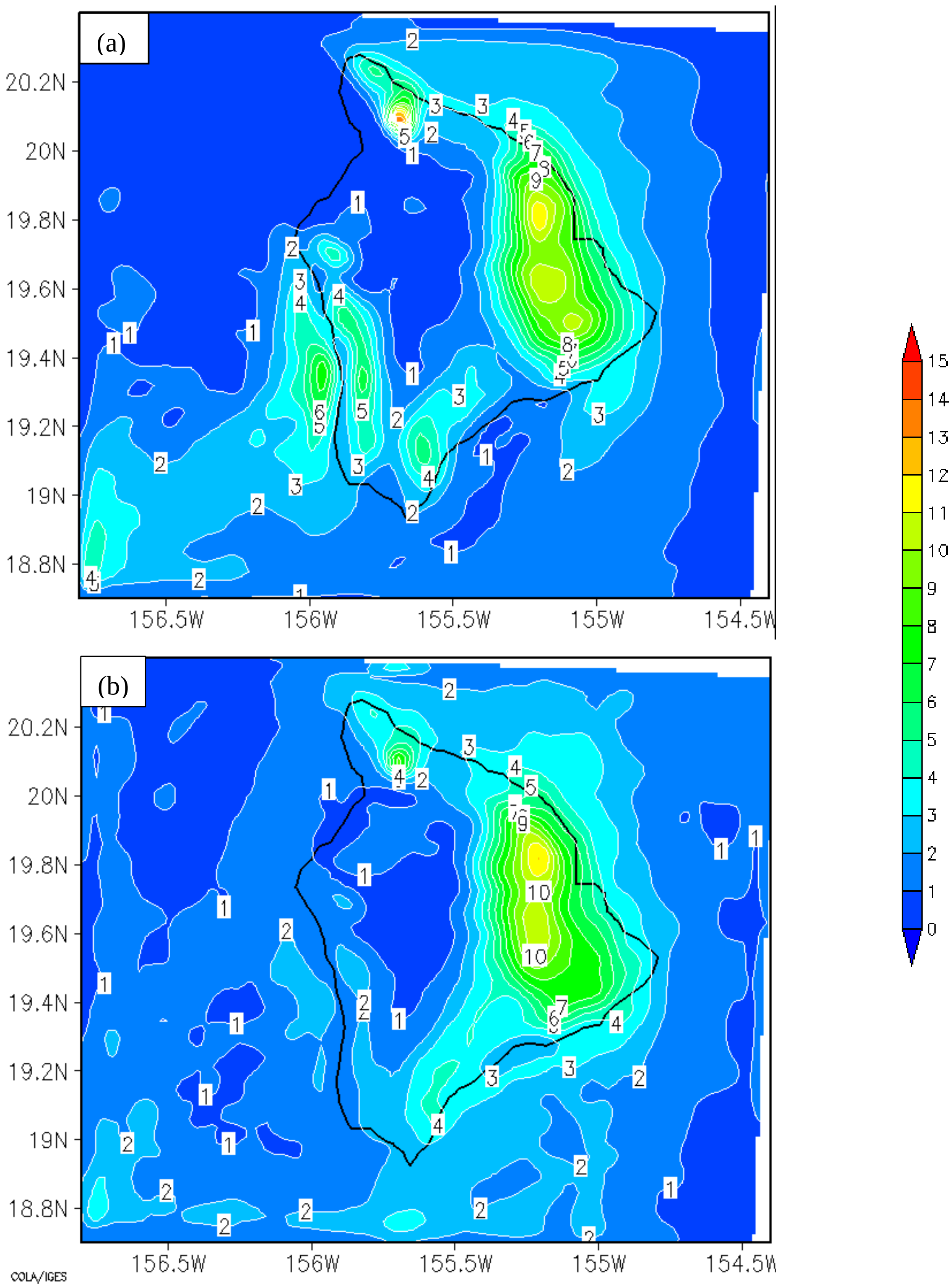

Fig. 3 The MM5/LSM simulated 6-year mean daily rainfall (mm) over Hawai'i during the (a) summer trade-wind days (b) winter months.

3.2 Simulated diurnal cycle

a) Thermodynamic variables

The diurnal variations of thermodynamic variables, winds, and rainfall are closely related to the diurnal heating cycle. There are differences in diurnal variations of thermodynamic variables between summer and winter on the leeside of Hawai'i.

At 0200 HST, the simulated 2-m air temperatures over the ocean and on the Kona slopes during the summer trade-wind days are about 2℃ higher (Fig. 4a) than during the winter months. At 1400 HST, the simulated 2-m air temperatures (Fig. 4b) over the ocean during both seasons are about as the same as at 0200 HST for both seasons, respectively. However, the simulated air temperatures on the mountains, the Kau desert, and the leeside of Kohala in the afternoon during the summer trade-wind days are > 4℃ higher than during the winter months (Fig. 4b). It is apparent that the afternoon solar heating on the mountains and the adiabatic warming due to the descending air on the leeside of the Kohala Mountains and the southwestern corner in summer are more significant than in winter.

At 0200 HST, the simulated TPW maximum in the leeside occurs over the ocean adjoining the Kona coast during the summer trade-wind days and is 7 mm higher than during the winter months (Fig. 4c). The TPW maximum occurs there because of the convergence between two counter-rotating vortices (Smith and Grubišić 1993). Moreover, the convergence between the land breezes and the westerly reversed flow will result in a relatively moist environment there during the nighttime.

At 1400 HST, the simulated TPW maximum adjoining the Kona coast moves closer to the island, and it is higher (> 9 mm) during the summer trade-wind days than during the winter months (Fig. 4d). During the daytime, the TPW on the Kona slopes during the summer trade-wind days is higher than during the winter months.

b) Winds and vertical motion

At 0200 HST, the wind speeds decrease significantly from > 6 m s^{-1} upstream to less than 0.5 m s^{-1} northeast of the island during the summer trade-wind days (Fig. 5a), and from about 4 m s^{-1} to less than 0.5 m s^{-1} during the winter months (Fig. 5b). The simulated winds are deflected northeast of the island in both summer and winter. The wind speeds at both the northern and southern tips during the summer trade-wind days (> 10 m s^{-1}) (Fig. 5a) are higher than during the winter months (7 m s^{-1}) (Fig. 5b). Moreover, the westerly reversed flow is stronger during the summer trade-wind days (~ 2.5 m s^{-1}) (Fig. 5a) than during the winter months (~ 1 m s^{-1}) (Fig. 5b). The westerly reversed flow is stronger during the summer trade-wind days than during the winter months because of stronger incoming winds upstream in summer.

At 1400 HST, the simulated wind speeds decrease significantly from > 6 m s^{-1} upstream to about 3 m s^{-1} northeast of the island during the summer trade-wind days (Fig. 5c) and from about 4 m s^{-1} to 2 m s^{-1} during the winter months (Fig. 5d), respectively. The simulated winds on the windward side at 1400 HST are weaker than 0200 HST because of the sea breeze is stronger at 1400 HST. The westerly reversed flow at 1400 HST is about 3 m s^{-1} during the summer trade-wind days and 1.5 m s^{-1} during the winter months.

The flow deceleration upstream is stronger at night (Figs. 5a and 5b) than during the daytime (Figs. 5c and 5d) since the air is more stable in the boundary layer. The simulated winds at both the northern and southern tips at 1400 HST (Figs. 5c and 5d) in both seasons are not as strong as at 0200 HST (Figs 5a and 5b). However, the westerly reversed flow at 1400 HST is about 1 m s^{-1} stronger than 0200 HST during the summer trade-wind days, and 0.5 m s^{-1} stronger during the winter months. In the afternoon, the westerly reversed flow close to the coast is enhanced by sea breezes in response to daytime heating over the land.

Since the rainfall is related to the vertical motion, and the simulated rising motions has maximum along the wake zone at the 900-hPa levels, which is between the cloud base and TWI, the simulated spacial distribution of vertical motion at the 900-hPa level is analyzed for the Kona leeside area. The 6-year mean simulated vertical motion at the 900-hPa level in summer trade-wind days shows that the rising motions over the ocean just west of the Kona coast at 0200 HST (Fig. 6a), and they are more than 5 cm s^{-1} larger during the summer trade-wind days than during the winter months. This is because of stronger convergence between the westerly reversed flow and the land breezes in response to a stronger westerly reversed flow in summer (Figs. 5a and 5b).

At 1400 HST, the rising motions shift inland above the Kona slopes during the summer trade-wind days are 14 cm s^{-1} (Fig. 6b) larger than during the winter months. The rising motions above the Kona slopes during the summer trade-wind days are stronger than during the winter months because a stronger westerly reversed flow merges with the onshore flow, and is lifted by the orography.

c) Vertical Cross Sections

Vertical cross sections are analyzed to capture better the structure of three-dimensional thermally driven circulations and the westerly reversed flow adjacent to the Kona coast. The mixing ratio and zonal winds are shown along the meridional (156.3˚W) cross sections (Fig. 7a), and the airflow, relative humidity, and vertical motion are presented in the zonal (19.4˚N) cross section in the wake zone over Hawai'i. The cross section along 156.3˚W crosses the axis of the maximum westerly reversed flow. The cross section along 19.4˚N is approximately along the axis of the westerly reversed flow between two counter-rotating vortices during the summer trade-wind days.

Along 156.3˚W, at 0200 HST during the summer trade-wind days (Fig. 8a), the mean zonal winds have a maximum (> 3 m s^{-1}) near the surface around 19.5˚N. The zonal wind maximum at 0500 HST during the summer trade-wind days is 2 m s^{-1} larger than during the winter months (Fig. 8b) due to stronger mean incoming winds in summer. Besides, the mean mixing ratios (Fig. 8a) within the westerly reversed flow are more than 15 g kg^{-1} near the surface and about 11 g kg^{-1} at the 875-hPa level (the highest level of the westerly reversed flow). At 0200 HST during the winter months (Fig. 8b), the mixing ratios of the westerly reversed flow are about 12.5 g kg^{-1} near the surface and about 8 g kg^{-1} at the 825-hPa level. The mean mixing ratios in the lower levels are higher during the summer trade-wind days than during the winter months here not only because of warmer 2-m air temperatures (Fig. 2c).

At 1400 HST, the zonal wind maximum during the summer trade-wind days (Fig. 8c) reaches 3.5 m s^{-1} near the surface. In contrast, during the winter months (Fig. 8d), the zonal wind maximum is about 2 m s^{-1} around the 965-hPa level in the afternoon hour. At 1400 HST (Fig. 8c), the mixing ratios near the surface are about 14.5 g kg^{-1} in summer, and 12 g kg^{-1} in winter (Fig. 8d), respectively. Although the mixing ratios at 1400 HST for both seasons (Figs. 8c and 8d) are smaller than at 0200 HST (Figs. 8a and 8b), the more moisture advects inland at 1400 HST due to stronger westerly winds (Figs. 8c and 8d).

At 0200 HST, the circulations on the leeside of the island along the zonal cross section at 19.4˚N (Fig. 7b) show that the rising motions during the summer trade-wind days (Fig. 9a) have a maximum (> 4 cm s^{-1}) over the ocean adjoining the Kona coast. Downslope winds (Fig. 9a) occur on the lower slopes because of nocturnal cooling. The circulations at 0200 HST during the summer trade-wind days (Fig. 9a) show that the rising motions just west of the Kona coast are a result of the convergence between the westerly reversed offshore flow and land breezes. The rising motions and the relative humidity maxima (Fig. 9a) are consistent with the rainfall maximum (Fig. 10a) over the ocean adjoining the Kona coast. During the winter months, the circulations at 0200 HST (Fig. 9b) show that the rising motions (> 2 cm s^{-1}) just west of the Kona coast is smaller than during the summer trade-wind days. The sinking motions (~ 4 cm s^{-1}) occur on the Kona lower slopes (Fig. 9b). With a stronger westerly reversed flow, the rising motions just west of the Kona coast during the summer trade-wind days (Fig. 9a) is stronger than during the winter months (Fig. 9b). In both seasons, the relative humidity maximum occurs just west of the Kona coast (Figs. 9a and 9b), due to the rising motions there in response to the convergence between westerly reversed flow and land breezes.

At 1400 HST during the summer trade-wind days (Fig. 9c), the strong westerly reversed flow merges with the onshore/upslope flow. The air is lifted on the Kona leeside slopes with rising motions (> 12 cm s^{-1}), and condenses over the lower Kona slopes. The circulation caused by orographic lifting has sinking motions over the ocean, and the subsidence causes the mixing ratio near surface at 1400 HST is lower than 0200 HST. During the winter months (Fig. 9d), the rising motions (> 6 cm s^{-1}) on the lower Kona slopes at 1400 HST are much smaller than during the summer trade-wind days because of a weaker and drier westerly reversed flow (Figs. 5c and 5d), and less pronounced solar heating on the slopes (Figs. 4a and 4b) during the winter months. Furthermore, the relative humidity maximum occurs on the Kona slopes in both seasons because orographic lifting.

d) Precipitation

During the summer trade-wind days, the simulated mean 3-hr accumulated rainfall at night from 0200 HST to 0500 HST (Fig. 10a) has a maximum over the ocean adjoining the Kona leeside (~ 1 mm). From 1400 HST to 1700 HST during the summer trade-wind days (Fig. 10c), the leeside rainfall maximum (~ 1.5 mm) occurs on the Kona lower slopes.

During the winter months, the 3-hr accumulated rainfall amount adjoining the Kona leeside coast from 0200 HST to 0500 HST (Fig. 10b) is relatively small (~ 0.2 mm). The 3-hr afternoon accumulated leeside rainfall maximum (~ 0.6 mm) occurs on the Kona slopes but is less than in summer (Fig. 10d).

The differences in the leeside rainfall amounts between summer and winter are related to a stronger westerly reversed flow caused by stronger incoming trade winds upstream and stronger diurnally driven winds with a higher moisture content during the summer trade-wind days than in winter months.

3.3 Summary

The simulated mean rainfall on the leeside over Hawai'i shows two maxima during the summer trade-wind days: one is over the ocean adjacent to the Kona coast at night, and the other is along the Kona lower slopes in the afternoon. However, there is no pronounced simulated mean rainfall maximum on the leeside over the island during the winter months.

More nocturnal rainfall adjoining the Kona coast on the leeside occurs during the summer trade-wind days than during the winter months due to a stronger westerly reversed flow with higher moisture content converging with the offshore flow. The afternoon rainfall maximum on the Kona lower slopes is more pronounced in summer than in winter because the stronger westerly reversed flow brings in higher moisture, and merges with the stronger upslope flow over the island in response to more significant solar heating.

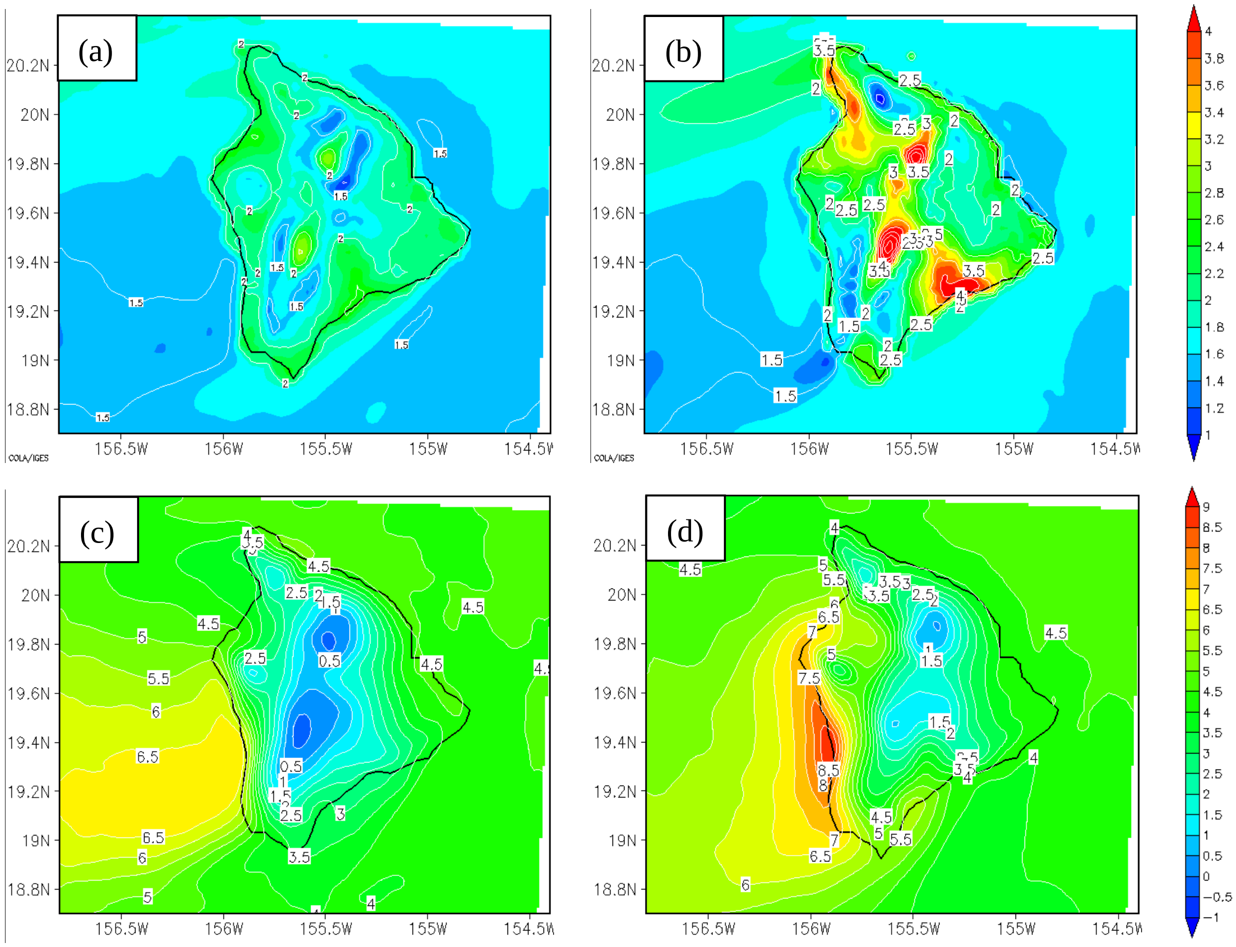

Fig. 4 The simulated 2-m air temperature differences (winter subtract from summer trade-wind days; ℃) at (a) 0500 HST, (b) 1400 HST; the simulated TPW (mm) differences (winter subtract from summer trade-wind days) at (c) 0500 HST, (d) 1400 HST over Hawai'i.

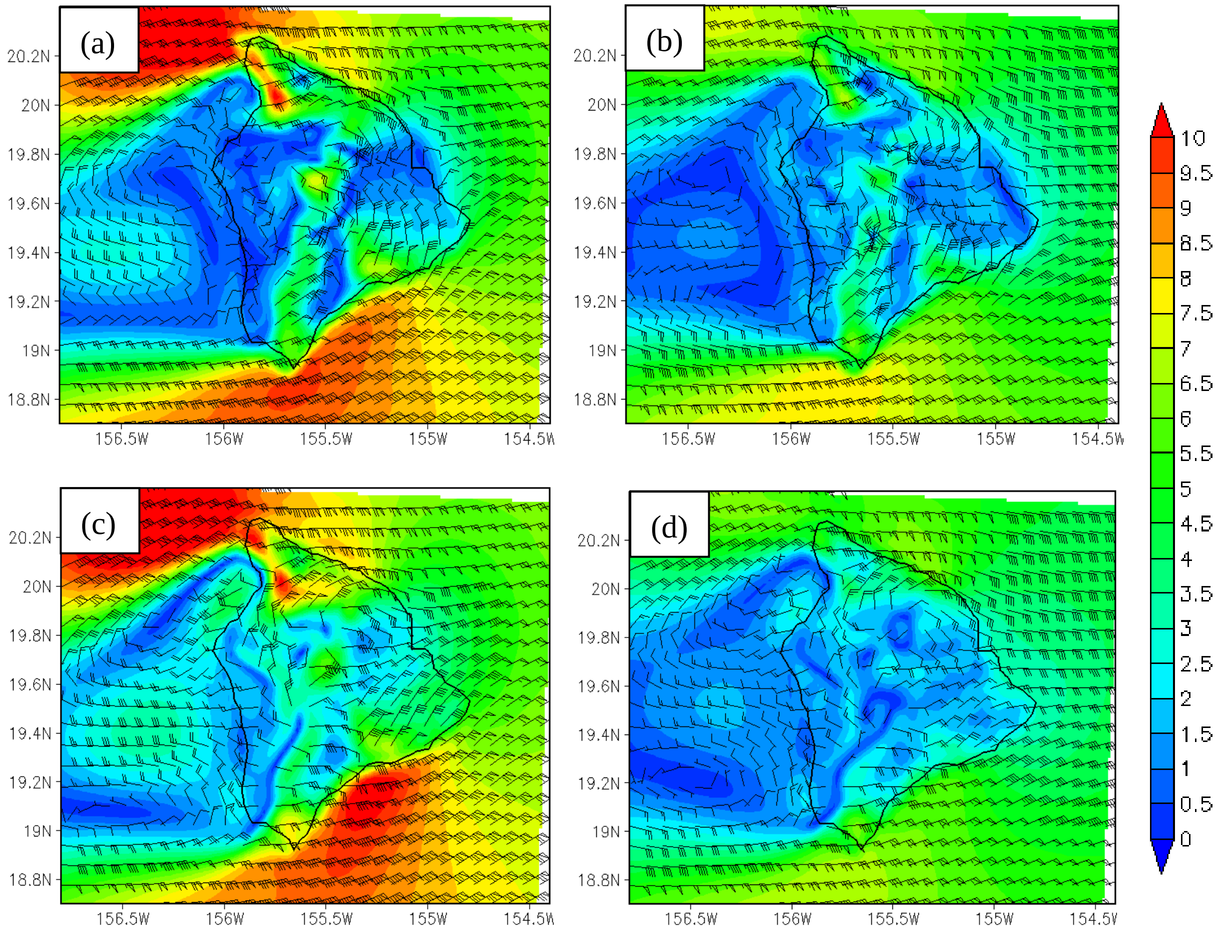

Fig. 5 The simulated mean 10-m wind (m s^{-1}; full barb: 1 m s^{-1}, pennant: 5 m s^{-1}) over Hawai'i during the summer trade-wind days at (a) 0500 HST, (c) 1400 HST, and during the winter months (b) 0500 HST, (d) 1400 HST.

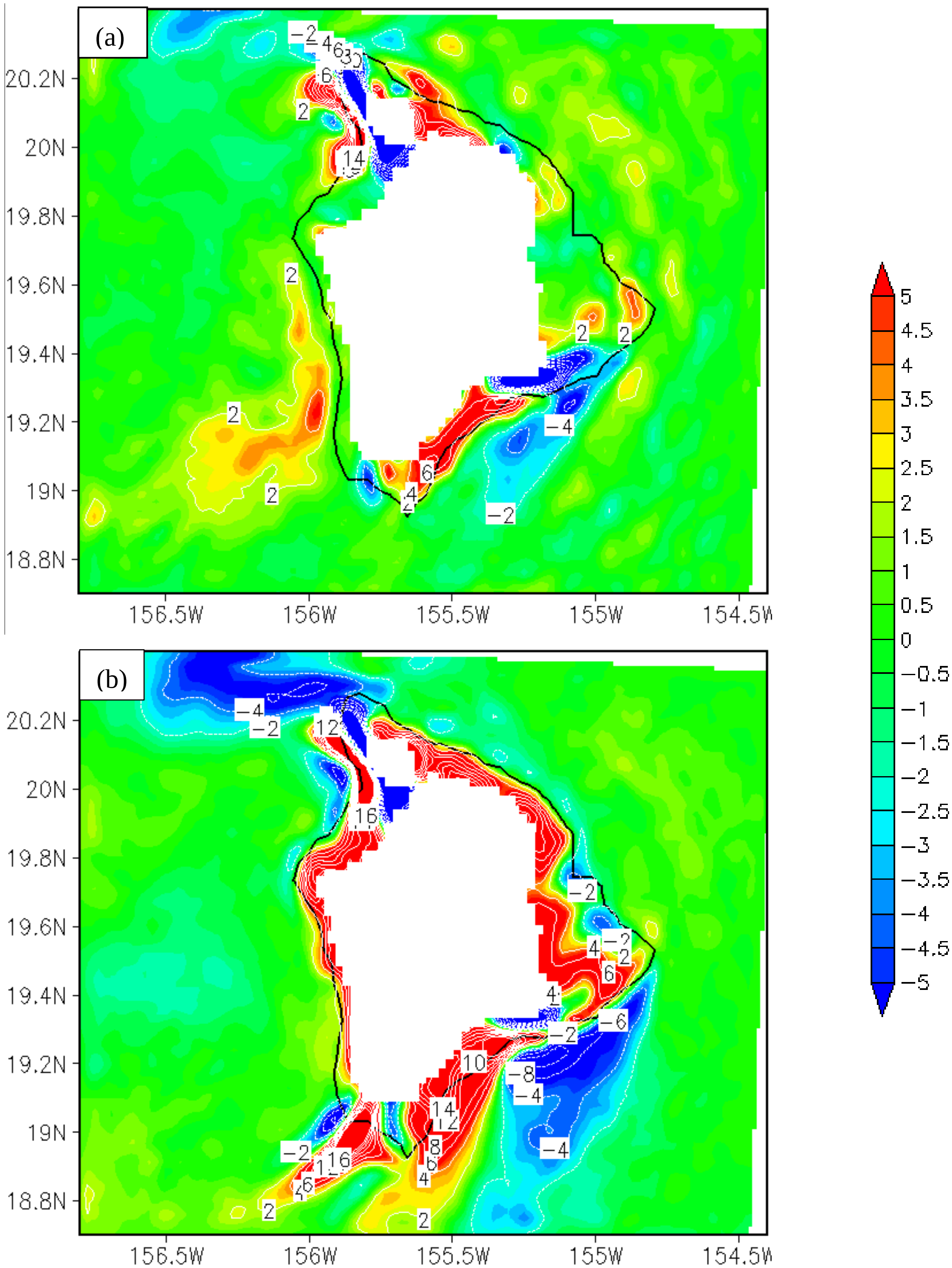

Fig. 6 The simulated mean 900-hPa vertical motion differences (winter subtract from summer trade-wind days) (cm s^{-1}) over Hawai'i at (a) 0500 HST, (b) 1400 HST.

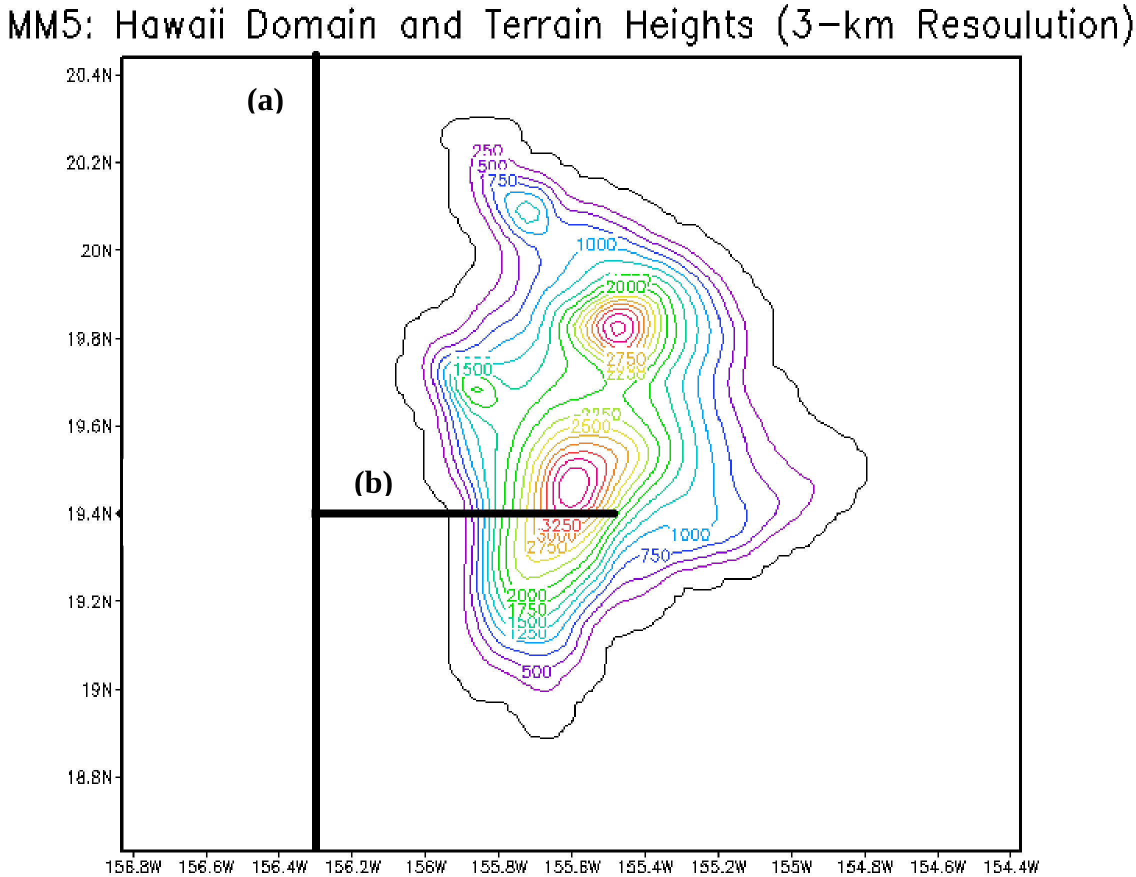

Fig. 7 The terrain heights in the simulation (contour; m), and cross sections along (a) 156.3W (from 18.7N to 20.4N), (b) 19.4 N (from 156.3W to 155.5W).

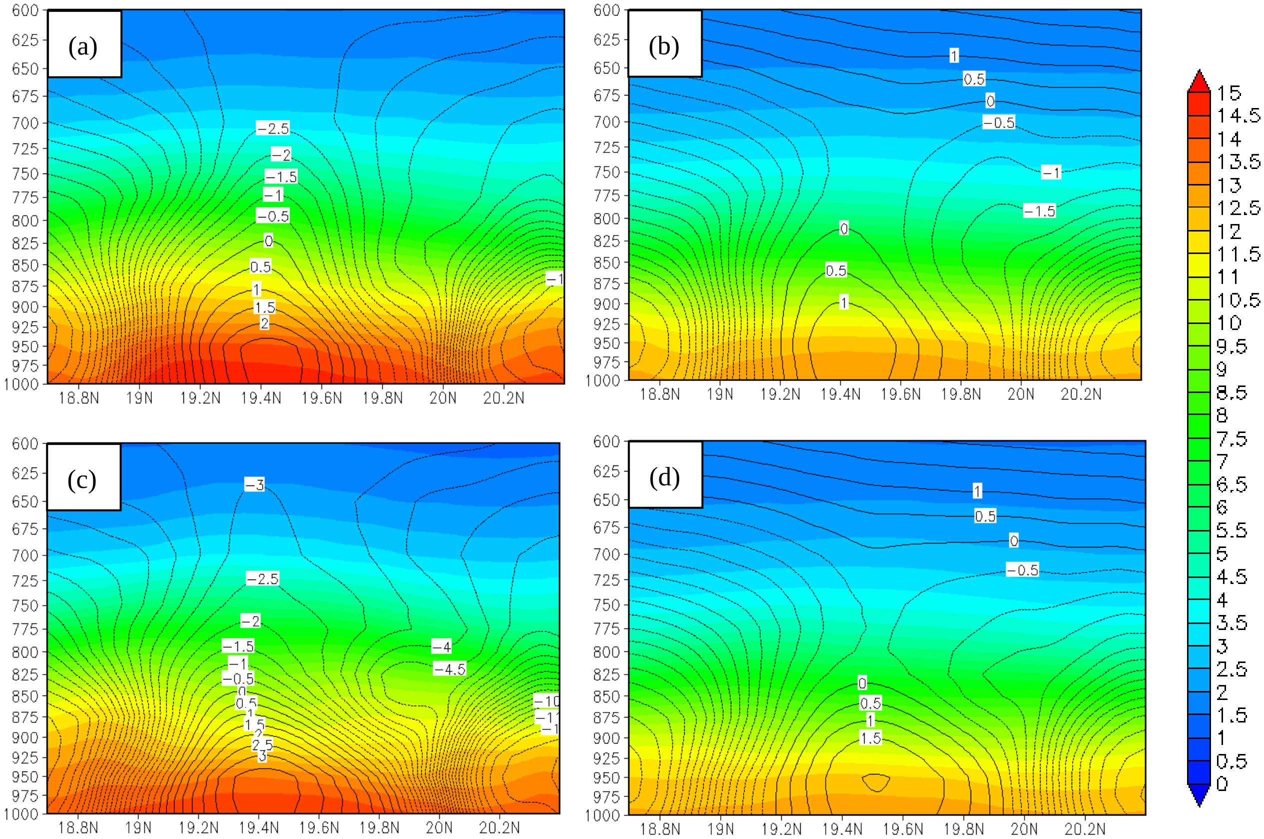

Fig. 8 The simulated mixing ratio (shaded; g kg^{-1}), and the zonal wind (contour; m s^{-1}) along the cross section (156.3˚W) over Hawai'i during the summer trade-wind days at (a) 0500 HST, (c) 1400 HST, and during the winter months at (b) 0500 HST, (d) 1400 HST.

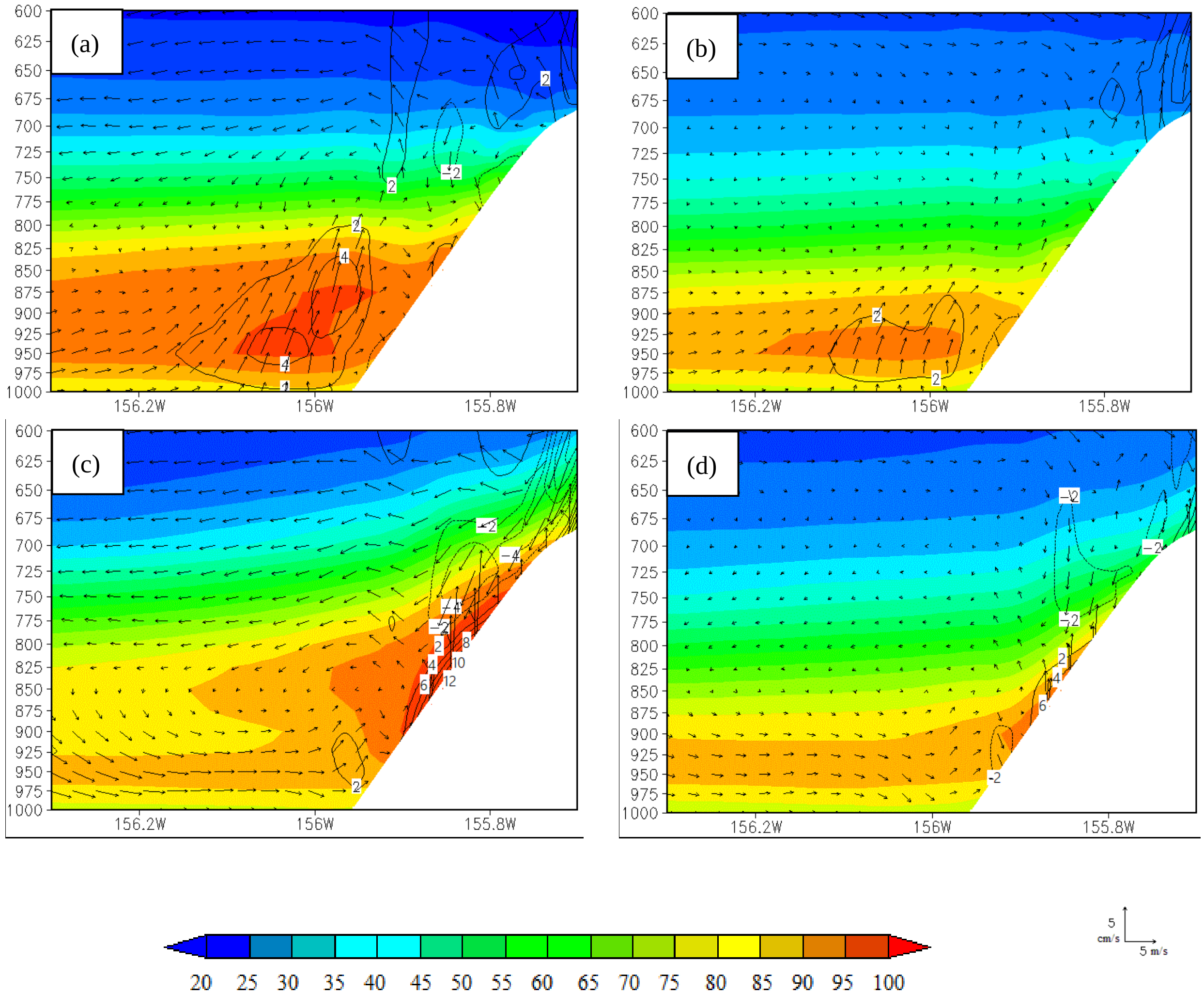

Fig. 9 The simulated relative humidity (shaded; %), the vertical motion (contour; cm s^{-1}), and the u-v winds (arrow) along the cross section (19.4°N) over Hawai'i during the summer trade-wind days at (a) 0500 HST, (c) 1400 HST, and during the winter months at (b) 0500 HST, (d) 1400 HST.

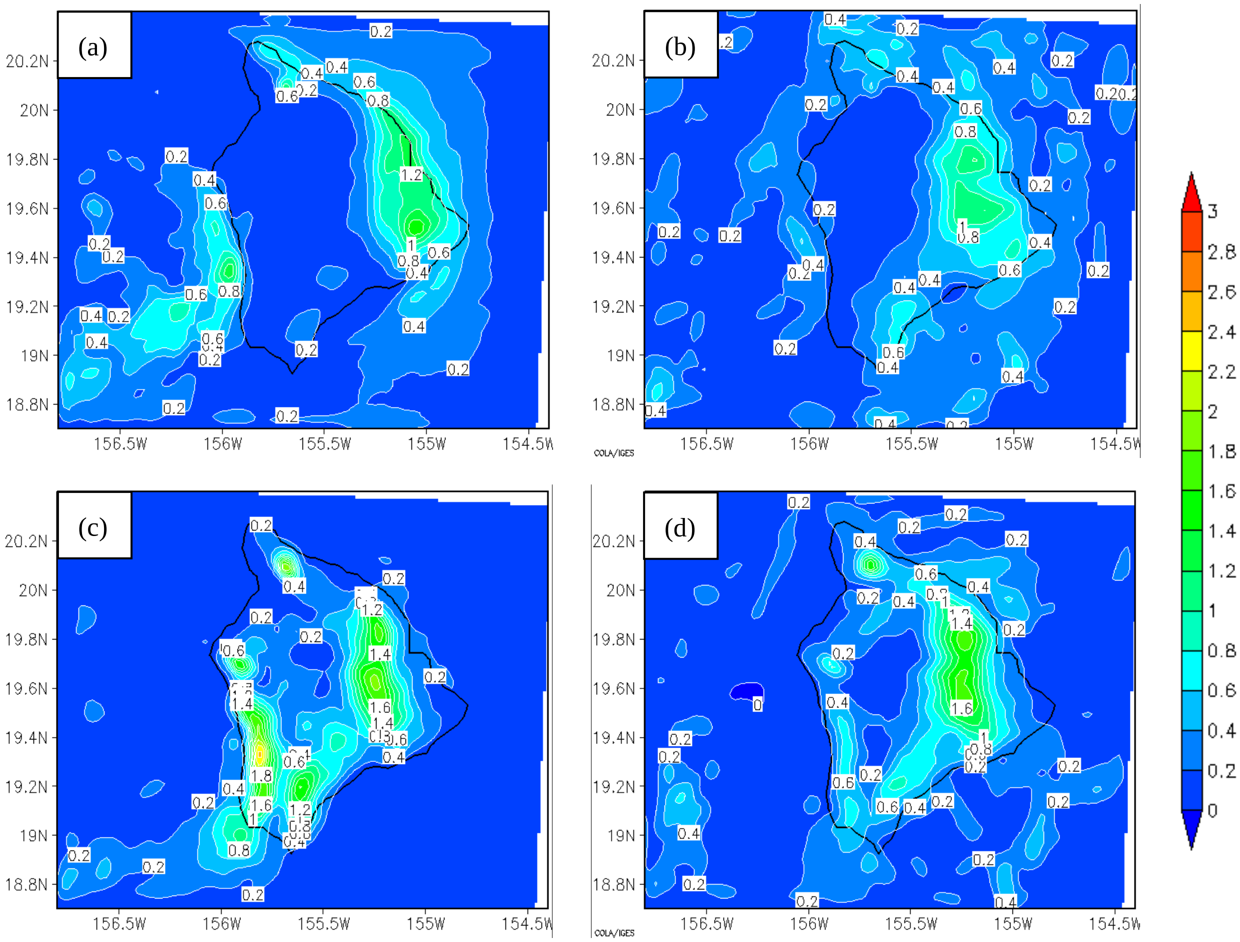

Fig. 10 The simulated mean 3-h accumulated rainfall (mm) over Hawai'i for the summer trade-wind days during (a) 0500 to 0800 HST, (c) 1400 to 1700 HST, and in the winter months during (b) 0500 to 0800 HST, (d) 1400 to 1700 HST.

CHAPTER 4

The Simulated Leeside Circulations under Winter Trade-wind Conditions over the Island of Hawai'i

From chapter 3, the stronger incoming winds and the higher moisture in summer than in winter are the reasons for summer leeside rainfall on the island of Hawai'i. However, during the wintertime, the trade wind flow is frequently interrupted by synoptic disturbances, e.g. cold fronts, upper-level troughs and Kona storms. With the synoptically disturbed days removed, the high-resolution model results will allow us to assess the impact of trade-wind conditions on island-scale weather and conditions, in particular on the leeside of Hawai'i more clearly than the winter mean fields. Since trade winds are persistent in summer, the rainfall, winds, and thermodynamic variables have little differences under the trade-wind conditions in summer and the summer mean. Thus, only the results under winter trade-wind conditions are shown in this chapter for comparison.

4.1 Simulated Mean State

The mean daily rainfall under the trade-wind conditions on the windward side is 3 mm larger than both seasons since the incoming northeasterly winds without synoptic disturbances are stronger with more significant orographic lifting. The double rainfall maxima on the leeside are evident under winter trade-wind conditions. Both daily leeside rainfall maxima (Fig. 11d) are about 4 mm lower than in the summer trade-wind days (Fig. 3a), but 1 mm higher than in the winter mean (Fig. 3b).

The simulated mean 10-m winds for the trade-wind days in winter show that the incoming winds are 1 m s^{-1} larger than in the summer trade-wind days (Fig. 11a), and 2.5 m s^{-1} greater than the winter mean (Fig. 11b), respectively. The simulated mean 10-m winds upstream under winter trade-wind conditions have a larger northerly wind component than in the winter mean (Fig. 11b). Under winter trade-wind days, the maximum westerly reversed flow are 1.5 m s^{-1} stronger than the winter mean (Fig. 11b). The westerly reversed flow maximum under winter trade-wind conditions is stronger compared to the summer mean, but the maximum area under winter trade-wind conditions is further (more western) from the Kona coast (Fig. 11a).

The TPW under the winter trade-wind conditions (Fig. 11c) show little difference from the winter mean. Although the incoming winds under winter trade-wind conditions (Fig. 11d) are about 1 m s^{-1} stronger than during the summer trade-wind days (Fig. 2a), the TPW on the Kona leeside under winter trade-wind conditions is 4 mm lower than during the summer trade-wind days. Comparing to the mean daily rainfall during the summer trade-wind days (Fig. 3a), the rainfall maxima on the Kona leeside for winter trade-wind days (Fig. 11d) are lower. It appears that the less rainfall on the leeside over Hawai'i is related to lower TPW in winter.

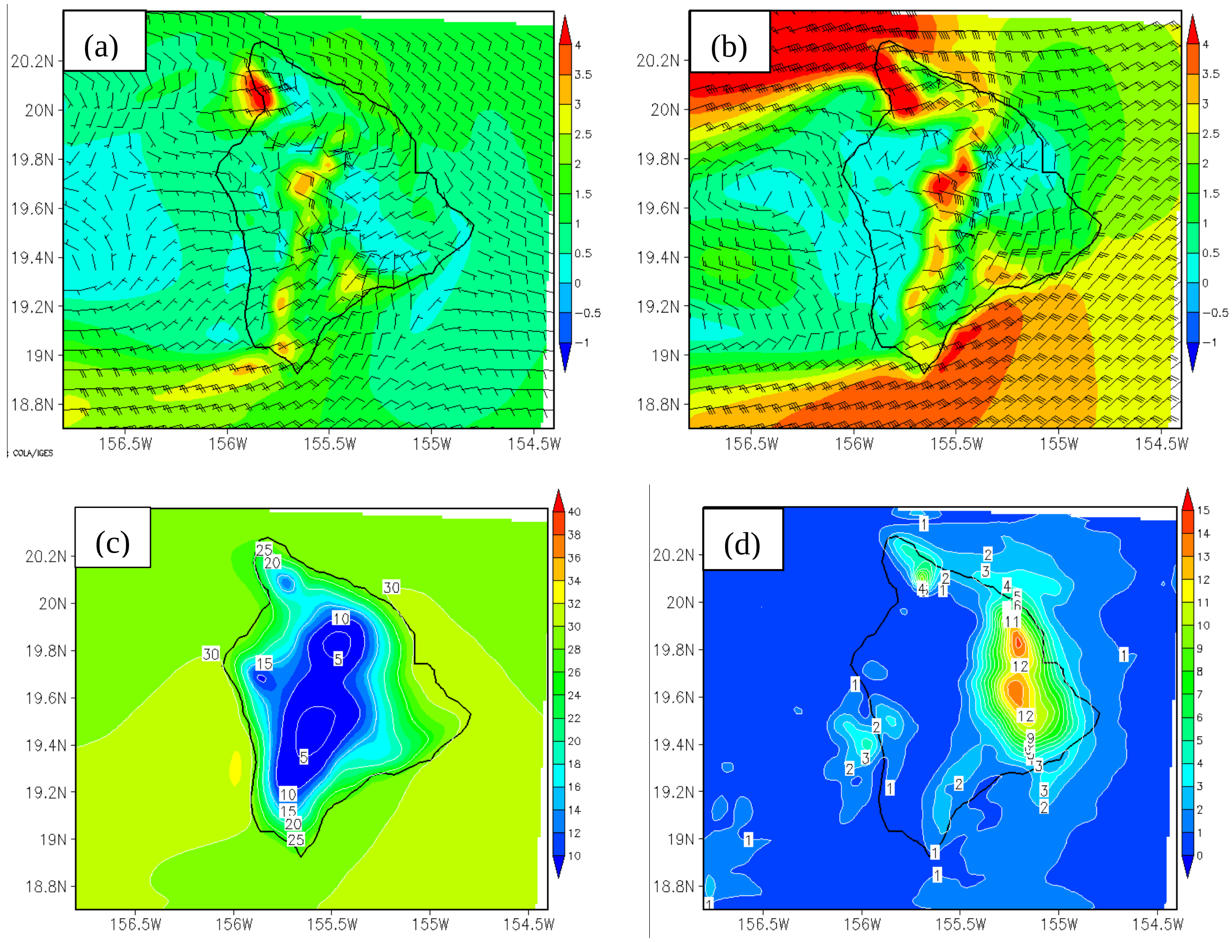

Fig. 11 The MM5/LSM simulation of the winter trade-wind days over Hawai'i: (a) 10-m wind (m s^{-1}; full barb: 1 m s^{-1}, pennant: 5 m s^{-1}) difference from summer (summer mean subtract from winter trade-wind days), (b) 10-m wind difference from winter (winter mean subtract from the winter trade-wind days), (c) TPW (mm), and (d) daily rainfall (mm).

4.2 Simulated diurnal cycle

Since there are only subtle differences in the diurnal thermodynamic variables between winter trade-wind conditions and the winter mean, the thermodynamics variables will not be discussed in this section.

a) Winds

The incoming winds at 0500 HST under the winter trade-wind days (Fig. 12a) are > 7 m s^{-1}, about 2.5 m s^{-1} higher than during the winter months, and about 1 m s^{-1} greater than during the summer trade-wind days. The westerly reversed flow maximum at 0500 HST under the winter trade-wind days (Fig. 12a), is 3 m s^{-1}, about 2 m s^{-1} higher than during the winter months, and 0.5 m s^{-1} greater than during the summer trade-wind days due to stronger incoming winds.

At 1400 HST, the incoming winds under the winter trade-wind conditions (Fig. 12b) are > 6.5 m s^{-1}, and the westerly reversed flow is about 2.5 m s^{-1}. The westerly reversed flow at 1400 HST under winter trade-wind conditions (Fig. 12b) is about 1.5 m s^{-1} higher than during the winter months. However, it is 0.5 m s^{-1} weaker than during the summer trade-wind days due to the westerly reversed flow merging with stronger sea breezes in response to more pronounced solar heating during the daytime in summer.

b) Vertical Cross Section

Along 156.3˚W (Fig. 7a), the zonal winds at 0500 HST under winter trade-wind conditions show that the westerly reversed flow has a maximum (~ 3 m s^{-1}) at the 975-hPa level around 19.4˚N (Fig. 13a). The westerly reversed flow maximum under winter trade-wind conditions (Fig. 13a) is 2 m s^{-1} larger than for the winter mean (Fig. 8b), and about the same as during the summer trade-wind days (Fig. 8a). The mixing ratio maximum (~ 12. 5 g kg^{-1}) under winter trade-wind conditions (Fig. 13a) is almost the same as in the winter mean (Fig. 8b), but 3.5 g kg^{-1} lower than the summer trade-wind days (Fig. 8a).

At 1400 HST, the westerly reversed flow maximum under winter trade-wind conditions is about 3 m s^{-1} at the 950-hPa level around 19.4˚N (Fig. 13b). It is 1 m s^{-1} larger than the winter mean (Fig. 8d), and 0.5 m s^{-1} smaller than the summer trade-wind days (Fig. 8c), respectively. The mixing ratio maximum (~ 12 g kg^{-1}) under winter trade-wind conditions (Fig. 13b) is almost the same as during the winter mean (Fig. 8d), but 3.5 g kg^{-1} lower than during the summer trade-wind days (Fig. 8c).

Along 19.4˚N (Fig. 7b), the rising motions on the leeside just west of the Kona coast at 0500 HST under winter trade-wind conditions are > 2 cm s^{-1} (Fig. 13c). It is slightly larger than in the winter mean (Fig. 9b), and 2 cm s^{-1} smaller than during the summer trade-wind days (Fig. 9a), respectively. The relative humidity maximum (90%) for the winter trade-wind conditions (Fig. 13c) occurs adjacent to the Kona coast at the 950-hPa level. The area of rising motions (~ 2 cm s^{-1}) and relative humidity (90%) just west of the Kona coast at 0500 HST under the winter trade-wind days (Fig. 13c) are larger than the winter mean (Fig. 9b) due to stronger convergence between the westerly reversed flow and land breezes under winter trade-wind conditions.

At 1400 HST, the rising motions (> 6 cm s^{-1}) on the Kona slopes under winter trade-wind conditions (Fig. 13d) show little differences from the winter mean (Fig. 9d) because daytime heating over land during the trade-wind days in winter and the winter mean is almost the same. The relative humidity maximum (> 90 %) under winter trade-wind conditions occurs on the Kona slopes due to orographic lifting. However, the rising motions on the Kona slopes during the summer trade-wind days (Fig. 9c) are larger than under winter trade-wind conditions (Fig. 13d) because of a stronger and relatively moist westerly reversed flow and more significant orographic lifting in response to stronger daytime heating in summer.

c) Precipitation

Comparing to the simulated rainfall between 0200 HST and 0500 HST in the winter mean (Fig. 10b), the rainfall (1.2 mm) adjacent to the Kona coast under winter trade-wind conditions (Fig. 12c) is 0.8 mm higher. The stronger westerly reversed flow under winter trade-wind conditions than in the winter mean transports more moisture toward the island. The rainfall amount adjacent to the Kona coast at night under winter trade-wind conditions (Fig. 12c) is almost the same as during the summer trade-wind days (Fig. 10a), but the rainfall area is smaller under winter trade-wind days.

The rainfall amount (> 1 mm) over the Kona lower slopes from 1400 HST to 1700 HST under winter trade-wind conditions (Fig. 12d) is 0.6 mm higher than in the winter mean (Fig. 10d) because stronger westerly reversed flow transporting more moisture inland. The rainfall amount in the afternoon for the winter trade-wind days (Fig. 12d) is 1.2 mm lower than during the summer trade-wind days (Fig. 10c) because the moisture content is lower with less pronounced thermally driven upslope flow there in winter.

4.3 Summary

The rainfall adjoining the Kona coast is more pronounced under winter trade-wind conditions than in the winter mean because of a more pronounced westerly reversed flow without the present of synoptic disturbances. Under winter trade-wind conditions, the convergence between the westerly reversed flow and land breezes is stronger than in the winter mean. There is little difference in thermally driven diurnal winds and moisture between the days under winter trade-wind conditions in winter and the winter mean. During the summer trade-wind days, with a higher moisture content than under winter trade-wind conditions, the rainfall adjoining the

Kona coast is greater. Moreover, the rising motions in response to the convergence between the westerly reversed flow and the land breezes during the summer trade-wind days is stronger than the trade-wind days in winter because the westerly reversed flow maximum is closer to the Kona coast.

On the Kona lower slopes in the afternoon hours, the 6-yr mean rainfall under winter trade-wind conditions is larger than in the winter mean because a stronger westerly reversed flow under winter trade-wind conditions brings more moisture inland. Under winter trade-wind conditions, the rainfall amount on the Kona slopes in the afternoon is lower than during the summer trade-wind days because of a lower moisture content and weaker orographic lifting in response to less significant daytime heating over land.

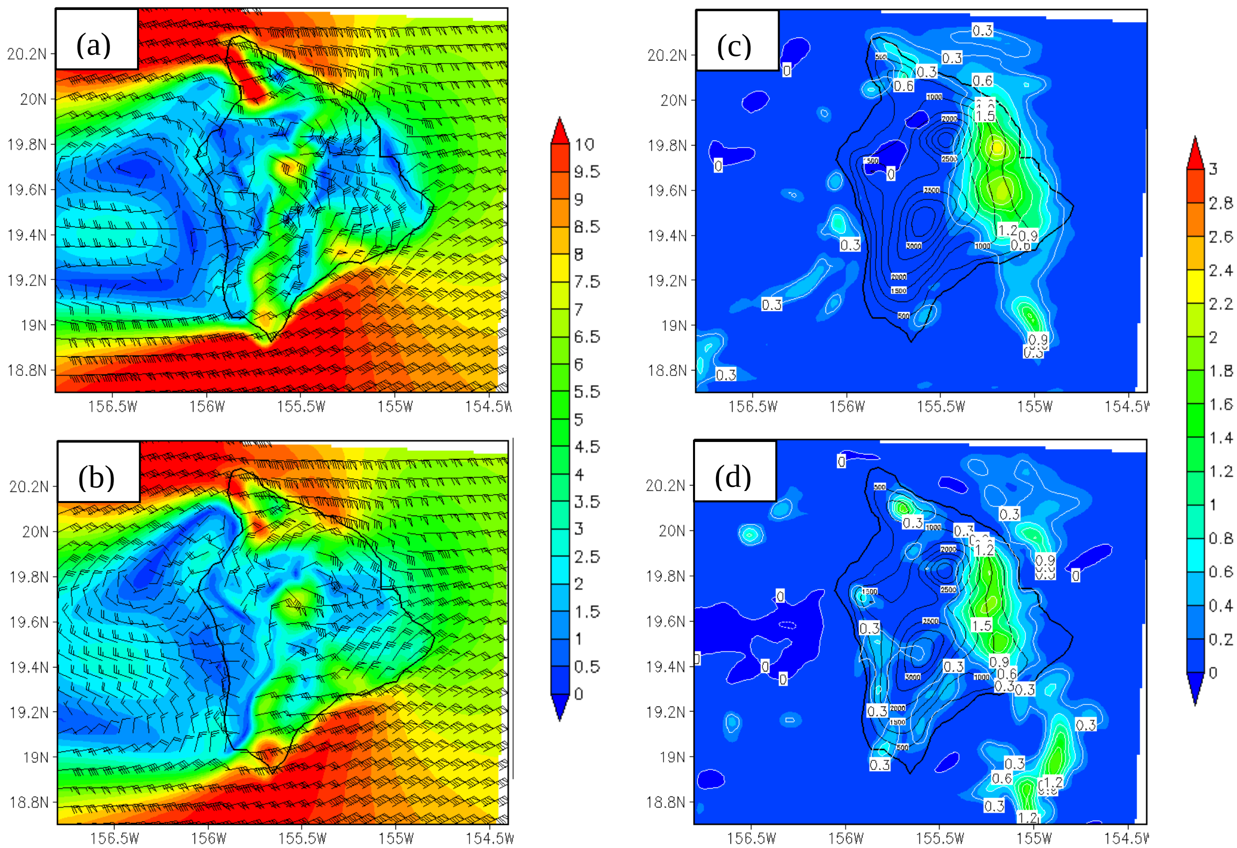

Fig. 12 The simulation of the winter trade-wind days over Hawai'i: 10-m wind (m s^{-1}; full barb: 1 m s^{-1}, pennant: 5 m s^{-1}) at (a) 0500 HST, (b) 1400 HST; the mean 3-h accumulated rainfall (mm) and the altitude (m; black contour with CI = 500 m) during: (a) 0500 HST to 0800 HST, (b) 1400 HST to 1700 HST.

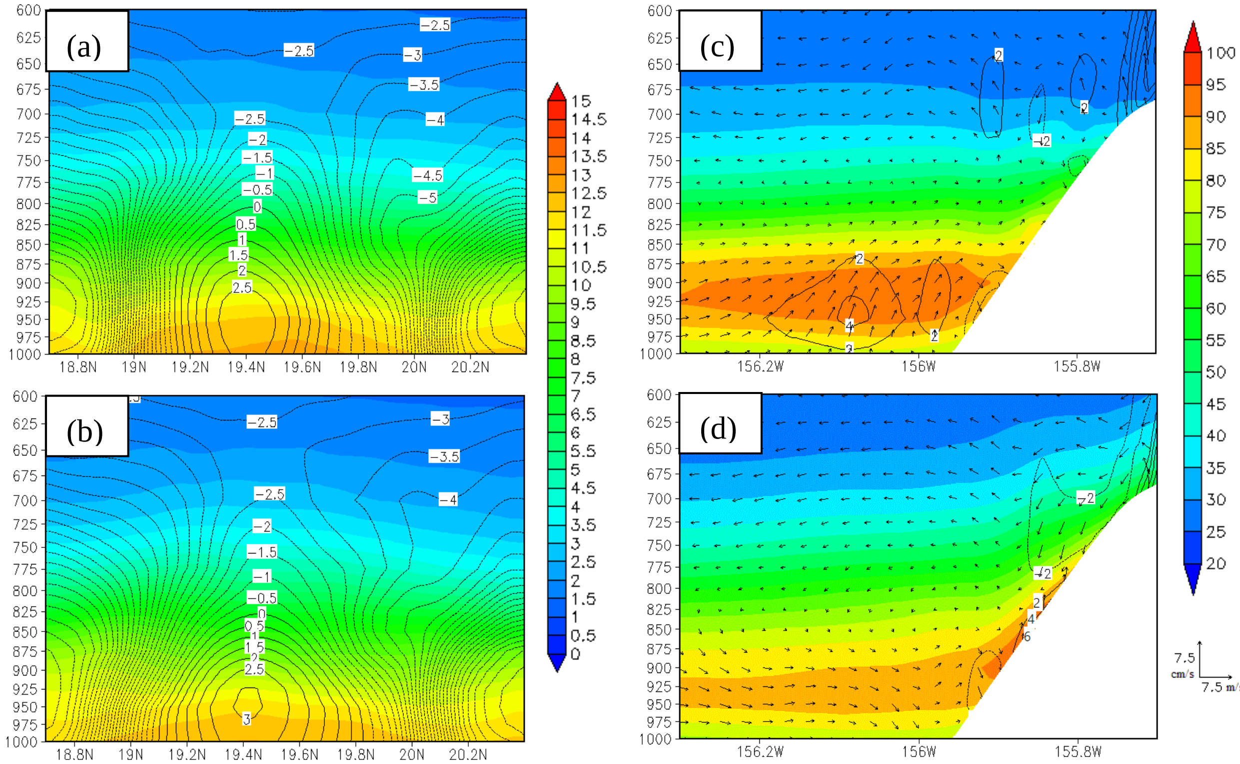

Fig. 13 The simulation of the winter trade-wind days over Hawai'i: along the cross section (156.3˚W), the simulated mixing ratio (shaded; g kg^{-1}), and the zonal winds (contour; m s^{-1}) at (a) 0500 HST, (b) 1400 HST. Along the cross section (19.4˚N), relative humidity (shaded; %), the vertical motion (contour; cm s^{-1}), and the airflow (arrow) at (c) 0500 HST, (d) 1400 HST.

CHAPTER 5

A Comparison of Simulated Leeside Circulations in Summer between Oahu and Hawai'i

The previous chapters show that the westerly reversed flow and the moisture content just west of the Kona coast are critical for the summer leeside rainfall over the island of Hawai'i. The moist westerly reversed flow between the counter-vortices on the leeside is a result of blocking effect under a low Fr-number regime (Smolarkiewicz and Rotunno 1989; Carbone et al. 1998) with mountains heights well above the TWI (Leopold 1949; Chen and Feng 1995; Chen and Feng 2001). What will be the differences in the summer leeside rainfall between Oahu and Hawai'i?

From a combination of satellite observations and numerical simulation, Yang et al. (2008) proposed that the thermal advection from the island interior to the leeside offshore strongly affects the cloud formation in the wake over Oahu. They suggested that the warm advection in response to the radiation heating during the daytime decreases the air pressure downstream, and enhances low-level wind convergence in the wake zone. On the contrary, for Hawai'i, sea breezes enhance the westerly reversed flow, preventing warm air over the land from being advected into the wake adjacent to the Kona coast at low levels. The cloud frequency is relatively low in the cold wake of Hawai'i in the afternoon, but relatively high in the warm wake of Oahu (Yang et al. 2008). However, Nguyen et al. (2010) show dry conditions downstream over Oahu in the afternoon, which is not favorable for the formation of clouds.

To understand why there is little rainfall along the western coast of Oahu, the horizontal winds, vertical motion, and thermodynamics over Oahu will be analyzed, and compared with those over the island of Hawai'i in this chapter.

5.1 Simulated Mean State

a) Winds

The simulated mean 10-m winds during the summer trade-wind days over Oahu (Fig. 14a) are consistent with the results presented by Nguyen et al. (2010). With Fr ~ 1 (model mountain height > 650 m), orographic blocking is still evident on Oahu. The incoming winds are about 7 m s^{-1}, and decrease to 5 m s^{-1} northeast of the Ko'olau Mountains, but increase to 8.5 m s^{-1} at both the northwestern and southeastern corners over the ocean because of orographic blocking. Due to orographic effects and surface friction, the simulated 10-m winds are weaker over the island than over the open ocean. Comparing with the simulated mean 10-m winds over Hawai'i during the summer trade-wind days (Fig. 2a), the winds at both northwestern and southeastern tips over Oahu (Fig. 14a) are not as strong as over Hawai'i. Moreover, the mean 10-m winds on the leeside over Oahu have no westerly return flow (Fig. 14a).

b) Thermodynamic variables

Over Oahu, the simulated 2-m air temperatures show significant warming (26.5℃) on the leeside of Oahu expanding downstream (Fig. 14b). The simulated TPW over Oahu (Fig. 10c) shows higher TPW (~ 36 mm) on the windward side and lower TPW (~ 34 mm) on the leeside may in response to the adiabatic decent of dry air.

In contrast, warming and drying on the leeside over the island of Hawai'i (Fig. 2b) only occurs on the leeside of both the northern and the southern tips, where the mountains tops/ridges are below the TWI. For Hawaii, there are an air temperature minimum due to the evaporative cooling and a TPW maximum from the moist westerly reversed flow adjacent to the Kona coast. The leeside of Oahu is under relative warm and dry conditions.

c) Precipitation

The simulated daily rainfall accumulations by MM5/LSM for summer trade-wind days (June, July, and August) during 2004 to 2009 are consistent with the results from Nguyen et al. (2010). The simulated mean daily rainfall shows the existence of a rainfall maximum over the Ko'olau Mountains (> 15 mm) due to the interaction between the incoming trade winds and the orography (Fig. 14d). There is no secondary maximum rainfall along the western coast of the island, but on the crest of Waianae Mountain Range (Fig. 14d).

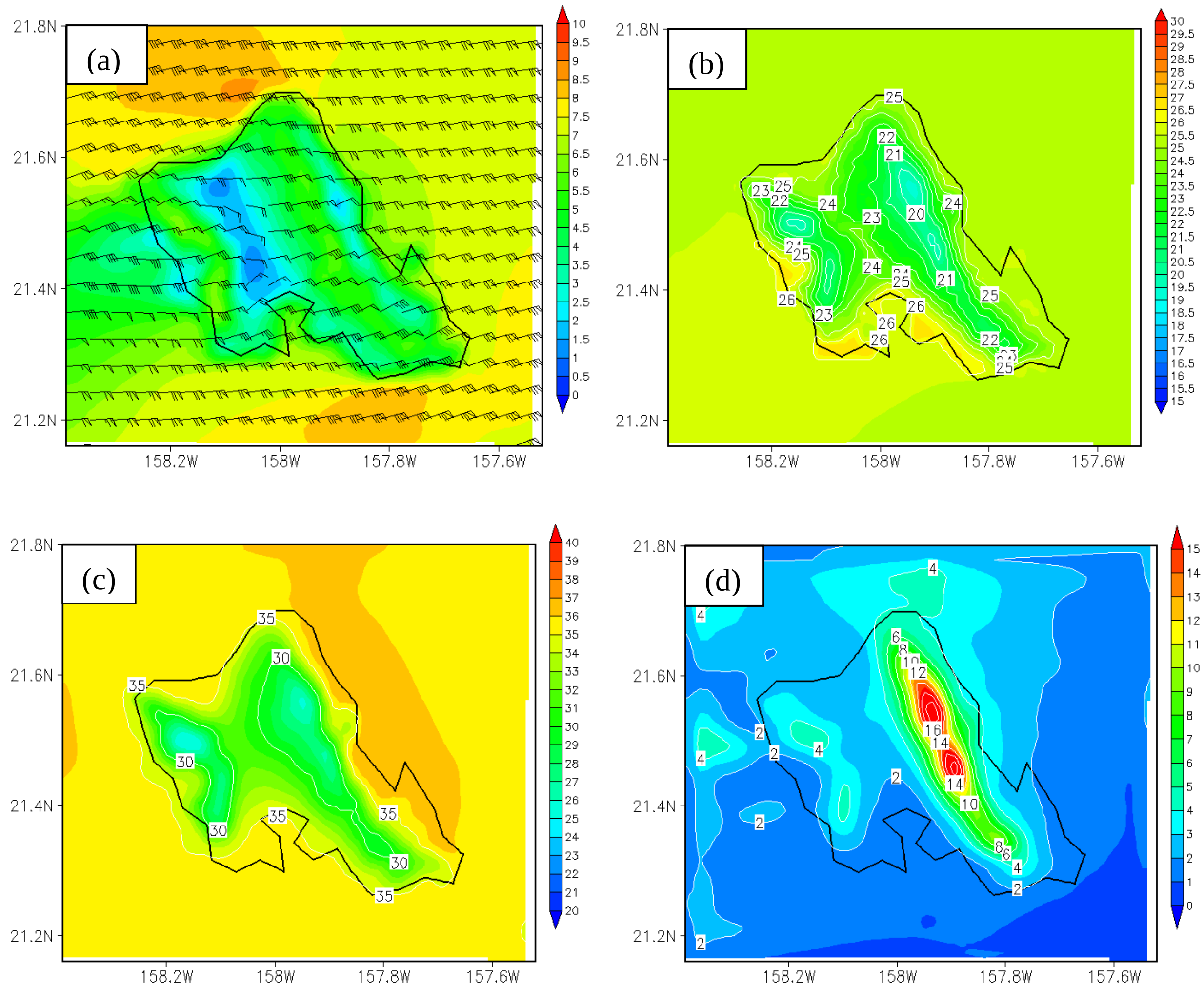

Fig. 14 The MM5/LSM simulated during the summer trade-wind days over Oahu (a) mean wind (m s^{-1}; full barb: 1 m s^{-1}, pennant: 5 m s^{-1}), (b) mean 2-m air temperature (℃), (c) mean TPW (mm), and (d) 6-yr mean daily rainfall (mm).

5.2 Simulated diurnal cycle

a) Thermodynamic variables

The simulated 2-m air temperatures at 0500 HST over the ocean and along the western coast of Oahu are about 25℃ (Fig. 15a). Different from the ocean just west of the Kona coast of Hawai'i (24℃), there is no temperature minimum over the ocean adjacent to the western coast of Oahu. At 1400 HST, the temperatures increase to 28℃ on the leeside of the Waianae Mountain Range and southern Oahu (Fig. 15b).

The simulated 900-hPa mixing ratio at 0500 HST (Fig. 15c) on the windward side of the Ko'olau Mountain Range is more than 12.5 g kg^{-1}, and decreases to less than 12 g kg^{-1} on the leeside of Ko'olau Mountain Range. It increases to 12 g kg^{-1} on the windward side of the Waianae Mountain Range due to orographic lifting, and drops to 10.5 g kg^{-1} on the leeside of the Waianae Mountain Range because of the adiabatic descent. At 1400 HST (Fig. 15d), the simulated 900-hPa mixing ratio shows less decrease on the both leeside of the mountains than at 0500 HST due to the stronger upslope flow in response to daytime heating in the afternoon. Moreover, the mixing ratio on the windward side of the Waianae Mountain Range at 1400 HST (12.5 g kg^{-1})(Fig. 15d) is larger than at 0500 HST (Fig. 15c) because of stronger orographic lifting. However, the drier conditions along the western coast of Oahu are evident at 1400 HST (Fig. 15d), although they are not as pronounced as at 0500 HST (Fig. 15c).

b) Winds

At 0500 HST, the simulated mean incoming winds at the surface during the summer trade-wind days (Fig. 16a) are about 7.5 m s^{-1}. The incoming winds decrease to 3.5 m s^{-1} to the northeast of the island, but increase to 8 m s^{-1} at both the northern and southern tips. The winds over the central Oahu are calm. Moreover, mountain winds are simulated on the windward side of the Waianae Mountain Range. On the leeside of the Waianae Mountain Range to the ocean, winds are easterly with speed from 3 m s^{-1} to 5 m s^{-1} (Fig. 16a).

At 1400 HST (Fig. 16b), the incoming winds are > 7 m s^{-1}, about 0.5 m s^{-1} weaker than at 0500 HST (Fig. 16a). They decrease to 4 m s^{-1} northeast of the island (Fig. 16b), which is 0.5 m s^{-1} stronger than 0500 HST (Fig. 16a). It is apparent that the flow deceleration in front of the island is more pronounced at night than the daytime. On the leeside of the Waianae Mountain Range, the wind speed in the afternoon (Fig. 16b) decreases to 0.5 m s^{-1} downstream due to surface friction and land surface heating. Although Nguyen et al. (2010) show afternoon sea breezes on the leeward of Oahu during July − August 2005, the afternoon onshore flow is absent in the 6-yr mean (Fig. 16b). It is interesting to note that the incoming winds at 1400 HST during July to August 2005 are 0.5 m s^{-1} weaker than 6-yr mean surface winds. The afternoon onshore flow along the leeside coast is simulated in Nguyen et al. (2010) may because trade winds were relatively weak in 2005.

At 0500 HST, the simulated 6-yr mean 900-hPa vertical motion (Fig. 16a) in summer shows rising motions on the windward side of the Ko'olau Mountain Range (~ 40 cm s^{-1}) and the Waianae Mountain Range (~ 20 cm s^{-1}). Sinking motions occur on the leeside of the Ko'olau Mountain Range (> 50 cm s^{-1}) and the Waianae Mountain Range (> 50 cm s^{-1}). Strong rising motions (> 50 cm s^{-1}) with Fr > 1 are shown on the leeside of the Waianae Mountain Range with Fr < 1 since the winds on the central Oahu are calm (Fig. 16a), which may indicate a hydraulic jump.

At 1400 HST, the 900-hPa vertical motion (Fig. 16b) shows that the rising motions are more than 30 cm s^{-1} and 20 cm s^{-1} on the windward side of the Ko'olau Mountain Range and the Waianae Mountain Range, respectively. The sinking motions are more than 50 cm s^{-1} and 40 cm s^{-1} on the leeside of the Ko'olau Mountain Range and the Waianae Mountain Range, respectively. At 1400 HST, the rising motions on the windward side of the Waianae Mountain Range are results of orographic lifting by the combined anabatic winds and trade wind aloft. At 0500 HST, the hydraulic jump behind the sinking motions on the leeside of the Waianae Mountain Range (> 40 cm s^{-1}) is stronger than at 1400 HST (> 20 cm s^{-1}).

The rising motions occur over the ocean adjoining the Kona coast at 0500 HST, and over the Kona slopes at 1400 HST during the summer trade-wind days. In contrast, the descending airflow on the west leeside is possibly followed by a hydraulic jump without a westerly reversed flow adjacent to the western coast of Oahu at both 0500 HST and 1400 HST.

c) Vertical Cross Sections

At 0500 HST, the vertical cross section of the easterly winds along 158.3˚W (Fig. 19a) shows a minimum (< 6 m s^{-1}) around 21.5˚N at lower levels adjacent to the western coast. The mixing ratios (Fig. 19a) show drier conditions (~ 13.5 g kg^{-1}) in lower levels between 21.4˚N to 21.6˚N adjacent to the western coast of Oahu because the moisture is removed due to orographic precipitation and the air descends on the leeside. At 1400 HST (Fig. 19b), the easterly winds have a minimum (1.5 m s^{-1}) near the surface adjacent to the western coast of Oahu. The easterly winds adjacent to the western coast at 1400 HST are much weaker than at 0500 HST.

The vertical cross section along 21.5˚N (Fig. 18b) is chosen because the simulated vertical motion maximum and rainfall maximum over the Waianae Mountain Range occur there, the highest point (Mt. Ka'ala) over Oahu. At 0500 HST (Fig. 19c), the easterly winds aloft pass over the island. Since Fr ~ 1 and the mountains over Oahu are lower than the TWI, the airflow aloft can cross over the mountains and descends on the leeside. The relative humidity (Fig. 19c) drops immediately at 0500 HST on both leeside of the Ko'olau Mountain Range (80%) and the Waianae Mountain Range (60%) because of the rain shadow effect and adiabatic descent. The relative humidity (Fig. 19c) shows dry condition on the western coast of Oahu.

At 1400 HST (Fig. 19d), in addition to the vertical motion, the relative humidity (Fig. 19d) shows 5% decrease from the windward side to the leeside of the Ko'olau Mountain Range. The relative humidity at 1400 HST (Fig. 19d) on the windward side of the Waianae Mountain Range is higher than at 0500 HST because of orographic lifting by the upslope flow combined with trade winds aloft. On the leeside of Waianae Mountain Range, the relative humidity at 1400 HST decreases, but not as much as at 0500 HST.

d) Precipitation

At 0500 HST, the simulated 3-hr accumulated rainfall maximum (> 2 mm) (Fig. 16a) over Oahu occurs on the ridge tops of the Ko'olau Mountains (Fig. 10a) due to the interaction of orography with incoming trade winds. Moreover, the nocturnal rainfall over the Ko'olau Mountain Range is also related to the cloud-top radiative cooling, the stronger rising motions with enhancing convergence due to the airflow deceleration, and a lower LFC at night (Nguyen et al. 2010).

At 1400 HST (Fig. 16b), in addition to 3-hr accumulated rainfall maximum (~ 1.2 mm) on the ridge of the Ko'olau Mountain Range, the second 3-hr accumulated rainfall maximum (> 1.2 mm) occurs over the peak of Ka'ala Mountain, the northern Waianae Mountain Range. The afternoon rainfall along the western coast of Oahu is possible only under weak and variable winds (Hartley and Chen 2010).

5.3 Summary

On Oahu, the airflows aloft can move over the mountains with Fr ~ 1. At night, the maximum rainfall occurs on the ridge tops of the Ko'olau Mountains because of the interaction between orography and trade winds. The relatively dry and warm conditions are present on the leeside of the Waianae Mountain Range over Oahu due to rain shadow effect. In contrast to the Kona Leeside of Hawai'i, although land breezes along the western coast are evident during the night in summer, without the presence of the moist westerly reversed flow, there is no nocturnal rainfall maximum offshore of the western leeside coast of Oahu.

At 1400 HST, the second rainfall maximum over Oahu occurs on the top of rather than on the leeside of the Waianae Mountain Range. The rainfall there results from orographic lifting by the combined upslope winds due to daytime heating and trade winds aloft on the windward slopes of the Waianae Mountain Range. Different from the lower Kona slopes over Hawai'i, orographic lifting with the combined moist westerly reversed is not evident on the western coast over Oahu. Therefore, the summer rainfall on the lower Kona slopes of Hawai'i is observed but not on the leeside of the Waianae Mountains over Oahu.

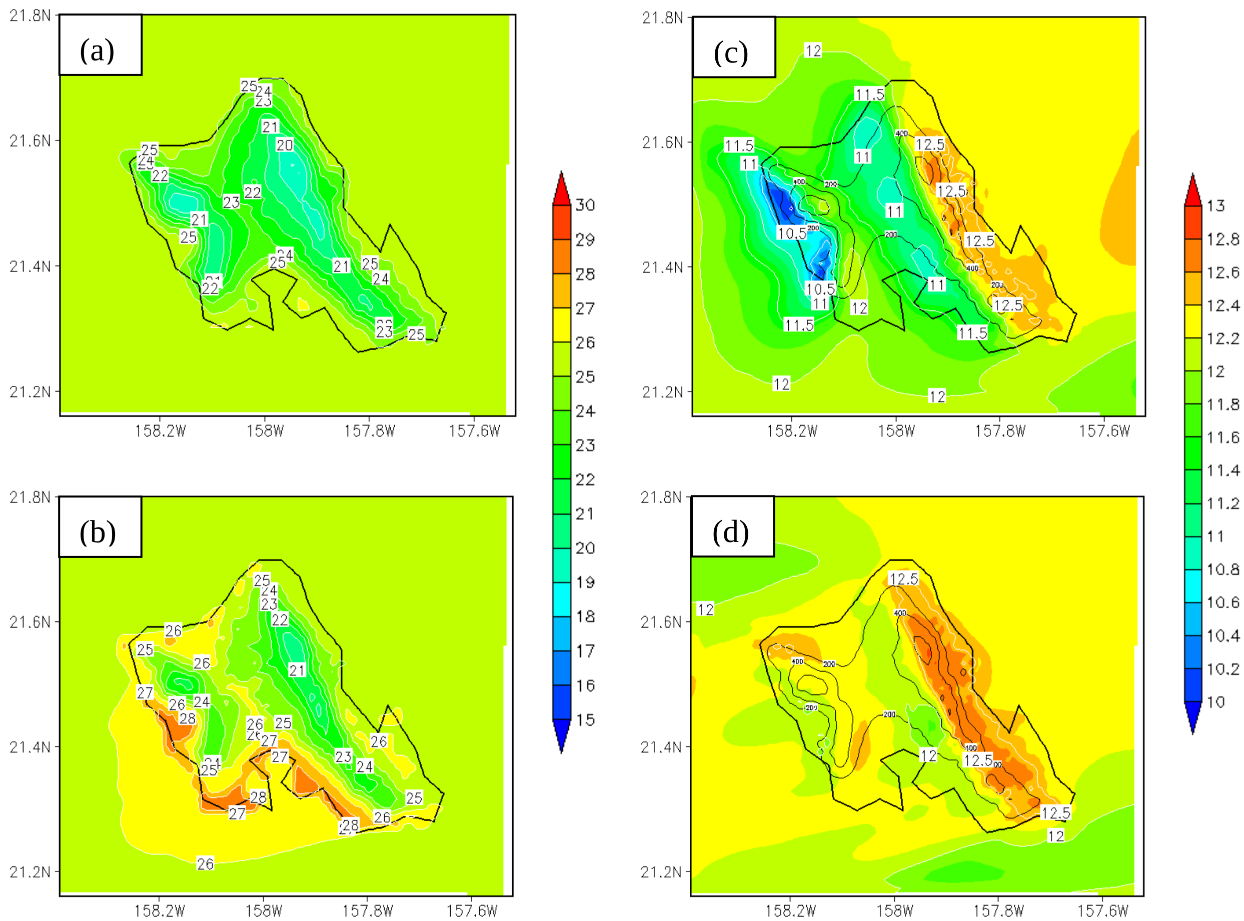

Fig. 15　The simulated mean 2-m air temperature (℃) over Oahu during the summer trade-wind days at (a) 0500 HST, (b) 1400 HST.　The simulated 900-hPa mixing ratio (g kg^{-1}; white contour and shaded) and altitude (m; black contour with CI = 200 m) over Oahu during the summer trade-wind days at (c) 0500 HST, (d) 1400 HST.

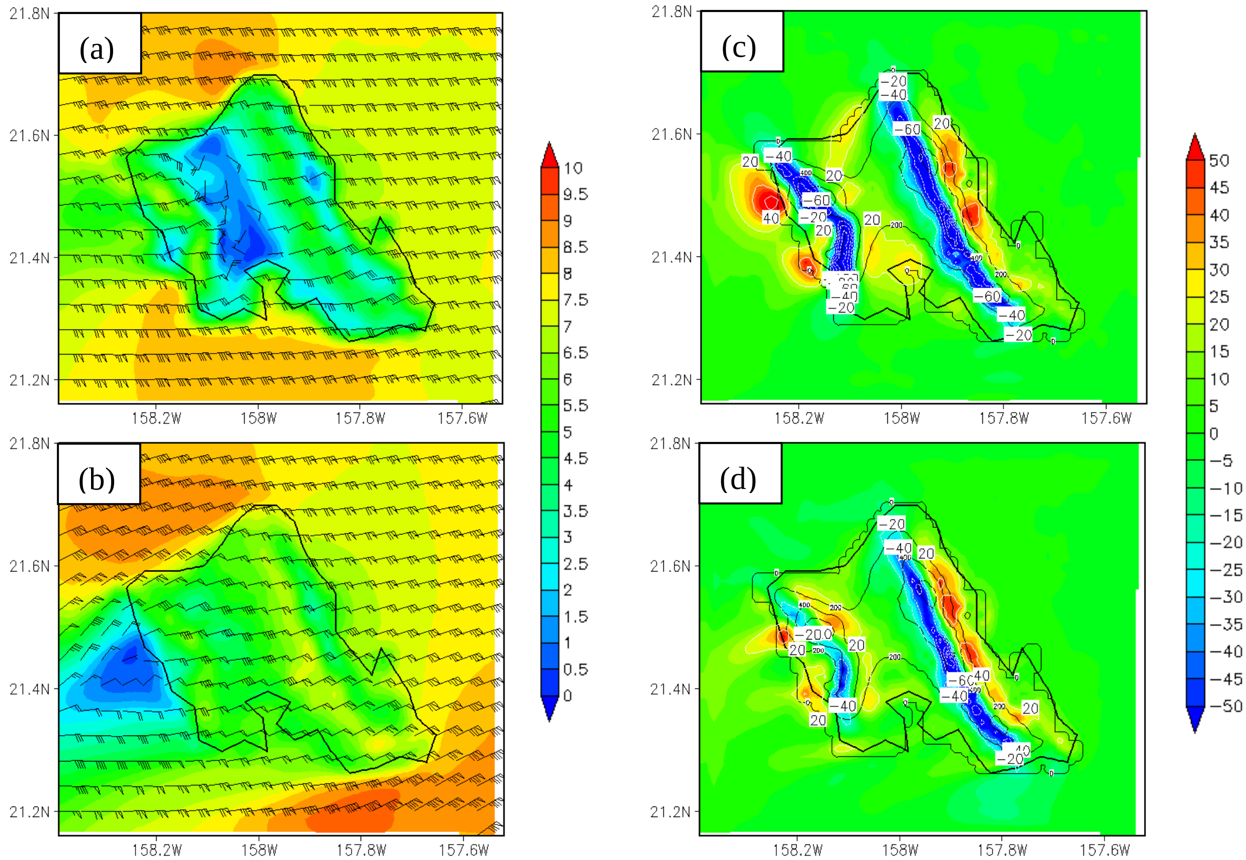

Fig. 16 The simulated 10-m wind (full barb: 1 m s^{-1}, pennant: 5 m s^{-1}) over Oahu during the summer trade-wind days at (a) 0500 HST, (b) 1400 HST. The simulated 900-hPa vertical motion (cm s^{-1}) and altitude (m; black contour with CI = 200 m) over Oahu during the summer trade-wind days at (c) 0500 HST, (d) 1400 HST.

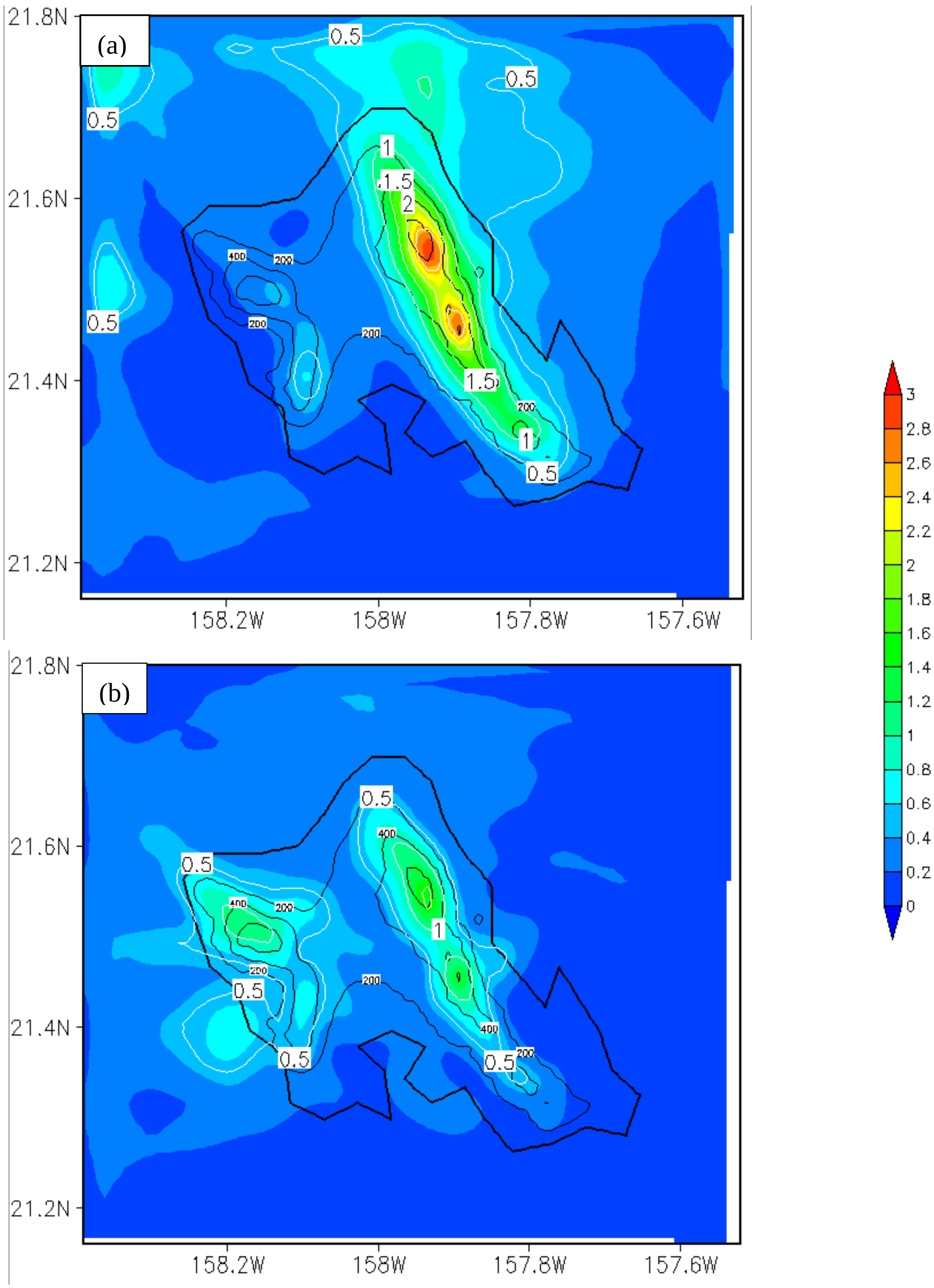

Fig. 17 The mean 3-h accumulated rainfall (mm) and altitude (m; black contour with CI = 200 m) over Oahu for the summer trade-wind days during (c) 0500 to 0800 HST, (d) 1400 to 1700 HST.

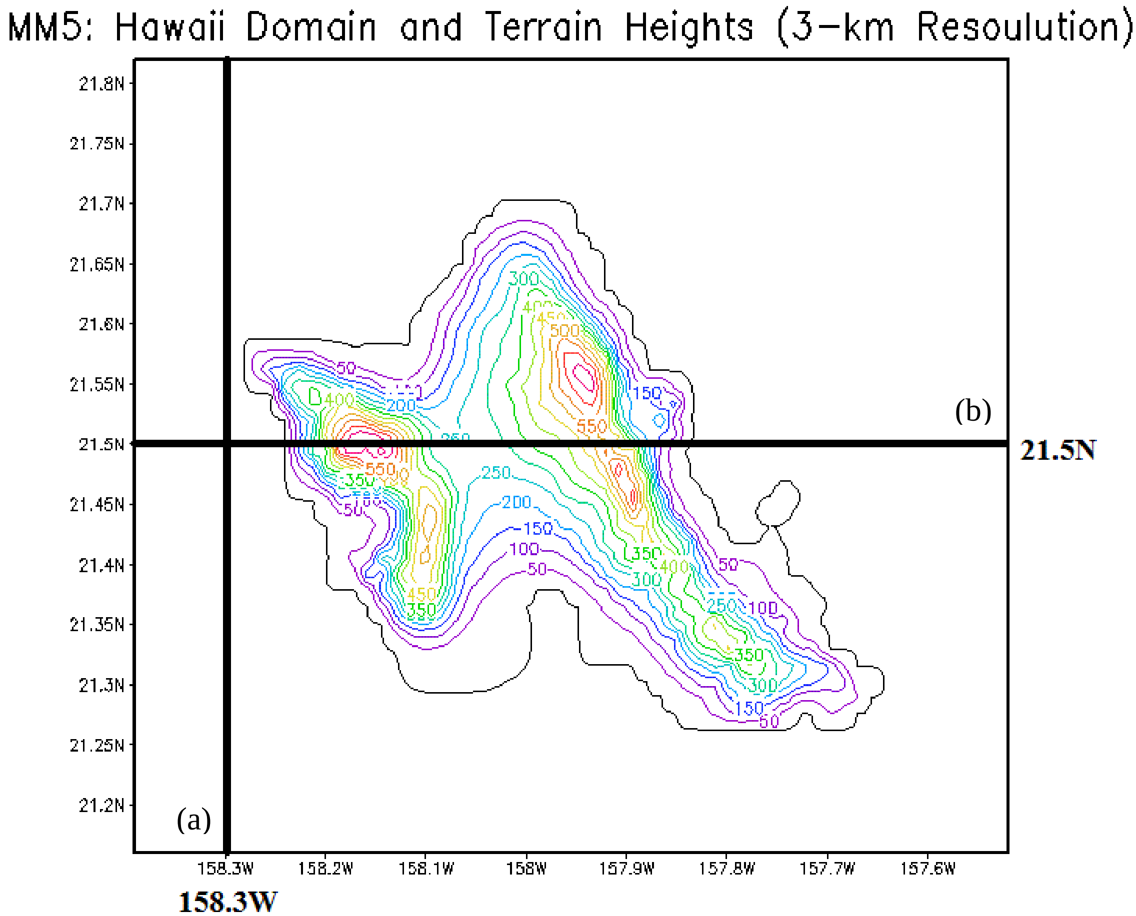

Fig. 18 The terrain height (contour; m) in the simulation, and the cross sections (a) 158.3W (from 21.16N to 21.8N), and (b) 21.5 N (from 157.52W to 158.39W)

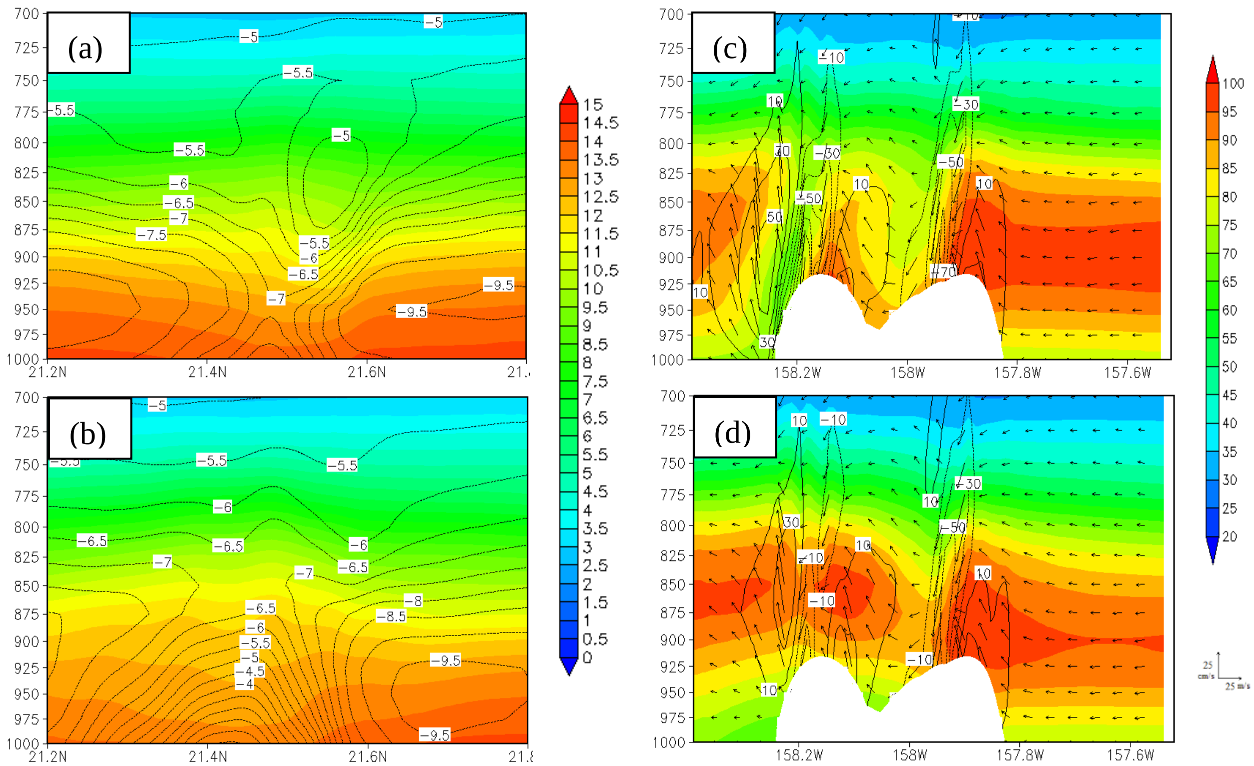

Fig. 19 The simulated mixing ratio (shaded; g kg^{-1}), and the zonal wind (contour; m s^{-1}) along the cross section (158.3˚W) at (a) 0500 HST, (b) 1400 HST during the summer trade-wind days over Oahu. The simulated relative humidity (shaded; %), the vertical motion (contour; cm s^{-1}), and airflow (arrow) the along the cross section (21.5N) at (c) 0500 HST, (d) 1400 HST during the summer trade-wind days over Oahu.

CHAPTER 6

Conclusion

6.1 Summary

To answer why the leeside rainfall maximum only occurs in summer over the island of Hawai'i, I compared the simulated diurnal leeside circulations during the summer trade-wind days with the winter months. The winter trade-wind days over Hawai'i are also studied. The archived daily MM5/LSM data of rainfall and airflow over the islands of Hawai'i from June 2004 to February 2010 are used.

For the island of Hawai'i, the mountain tops of Mauna Kea and Mauna Loa are well above the TWI with Fr ~ 0.3; therefore, upstream airflow splitting occurs with two contour-rotating vortices and a westerly reversed flow adjacent to the Kona leeside. There are two summer rainfall maxima identified on the western leeside of Hawaii. One occurs at night over the ocean adjacent to the Kona coast due to the convergence between the moist westerly reversed flow and land breezes. The other occurs in the afternoon on the Kona slopes due to orographic lifting by the combined moist westerly reversed flow and sea breezes.

At night, the rainfall along the west of the Kona coast in summer is more pronounced than in winter because the convergence between the moist westerly reversed flow and land breezes is stronger in summer. In the afternoon, the rainfall amount on the Kona slopes in summer is larger than in winter since orographic lifting is more pronounced in summer. Moreover, in summer, the moisture content in the lower layers in the westerly reversed flow is higher (> 2 g kg^{-1}) than in winter.

Although the incoming trade wind speeds in summer are slightly smaller than under the winter trade-wind days, the rainfall maximum adjoining the Kona coast at night in summer is higher because of higher moisture content associated with a westerly reversed flow. Under very similar thermal conditions between the winter trade-wind days and the winter mean, the rainfall amount adjoining the Kona coast for the winter trade-wind days is larger than the winter mean due to a stronger westerly reversed flow under winter trade-wind conditions. A comparison between the winter trade-wind days and the summer trade-wind days indicates that a higher moisture content and more significant orographic lifting play very important roles in the summer rainfall maximum on the Kona slopes over Hawai'i.

For Oahu, the mountains are well below the TWI with Fr ~ 1; therefore, the airflow aloft can cross the mountains and descend in the lee. It is apparent that the leeside rainfall over Oahu will be different from Hawai'i. The archives of 6-yr daily MM5/LSM data are also used to study rainfall, airflow, and thermodynamics over Oahu.

In contrast to Hawai'i, there is only one secondary rainfall maximum on the Ka'ala Mountain in the afternoon because of the orographic lifting by the combined trade wind aloft and the upslope winds. No rainfall maximum is simulated and observed along the western coast of Oahu except under weak and variable wind conditions. For the western leeside coast of Oahu, the environment is dry and warm due to the descending air and rain shadow effect in response to Fr ~ 1 and the fact that the mountains are lower than the TWI. Moreover, without a westerly reversed flow adjacent to the western coast of Oahu, the moisture cannot be brought to the western coast from the ocean.

6.2 Future work

The archives of daily real-time MM5/LSM for the Hawaiian Islands are helpful in understanding the weather and short-term climate over the Hawaiian Islands, especially the simulations are validated by observations. Those data can be used to provide more insight into the airflow and island-scale weather conditions over Hawaiian Islands from 2004 to 2010.

An additional study that needs to be completed is the comparison in instability in the Kona area between the summer trade-wind days, the winter months, and the winter trade-wind conditions. For the warmer, moister westerly reversed flow on the Kona leeside in summer, the air within the marine boundary layer may be more unstable during the summer than the winter trade-wind conditions. CAPE or convective instability could possibly be used.

In my study over Oahu, the 6-yr mean simulated surface winds show no the westerly reversed flow adjacent to the western leeside in the afternoon during the summer trade-wind days. However, the westerly reversed flow occurs in the afternoon from the simulation during July and August 2005. The differences could possibly related differences in trade wind speeds. I will investigate the island-scale circulations and rainfall under different trade-wind conditions for Oahu in the future.

Further studies could be done in understand the rainfall over the Hawaiian Islands by comparing different conditions. A comparison in the special and temporal distributions of rainfall over Hawaiian Islands between trade-wind conditions and the synoptic-scale disturbance would be studied. Moreover, the rainfall associates El Niño over Hawaiian Islands could be studied since there are two weak El Niño, one moderate El Niño, and one moderate La Niña events during 2004 to 2010.

Appendix A: The Mean Diurnal Cycle with 3-hr Interval during the Summer Months

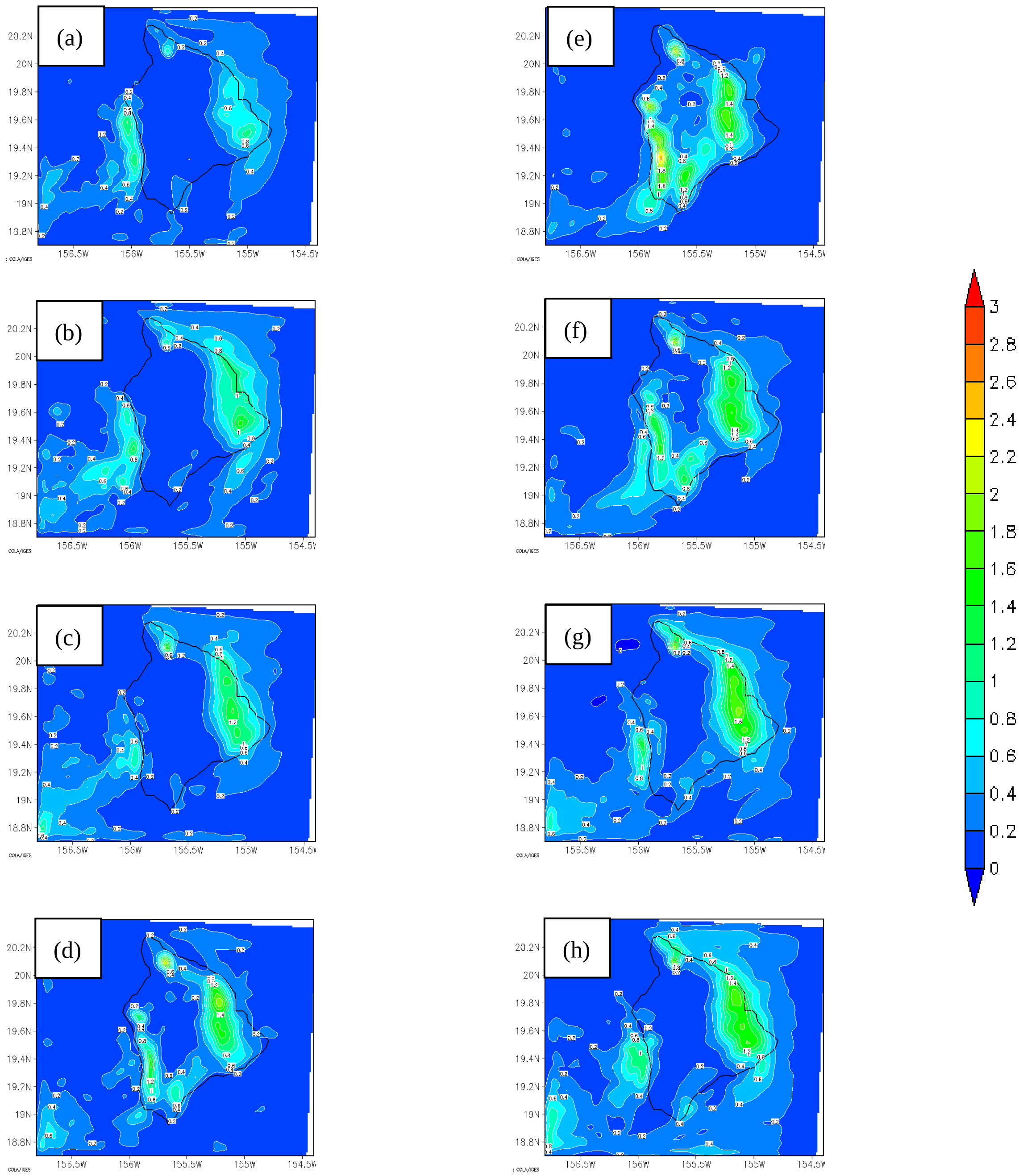

A 1 The simulated mean 3-h accumulated rainfall (mm) over Hawai'i in the summer months during (a) 1100-0200 HST, (b) 0200-0500 HST, (c) 0500-0800 HST, (d) 0800-1100 HST, (e) 1100-1400 HST, (f) 1400-1700 HST, (g) 1700-2000 HST, and (h) 2000-2300 HST.

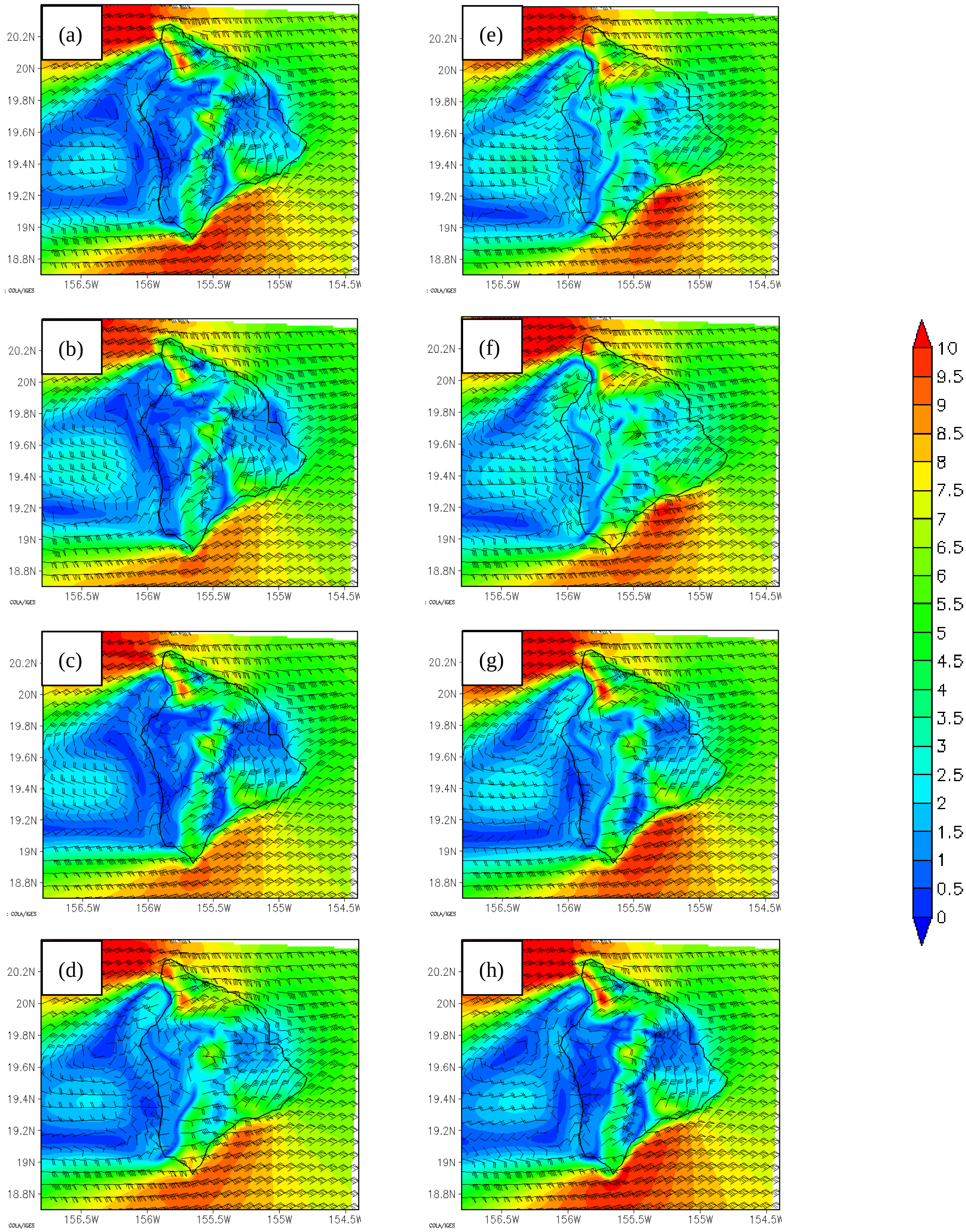

A 2 The simulated mean diurnal wind (m s^{-1}; full barb: 1 m s^{-1}, pennant: 5 m s^{-1}) over Hawai'i during the summer months at (a) 0200 HST, (b) 0500 HST, (c) 0800 HST, (d) 1100 HST, (e) 1400 HST, (f) 1700 HST, (g) 2000 HST, and (h) 2300 HST.

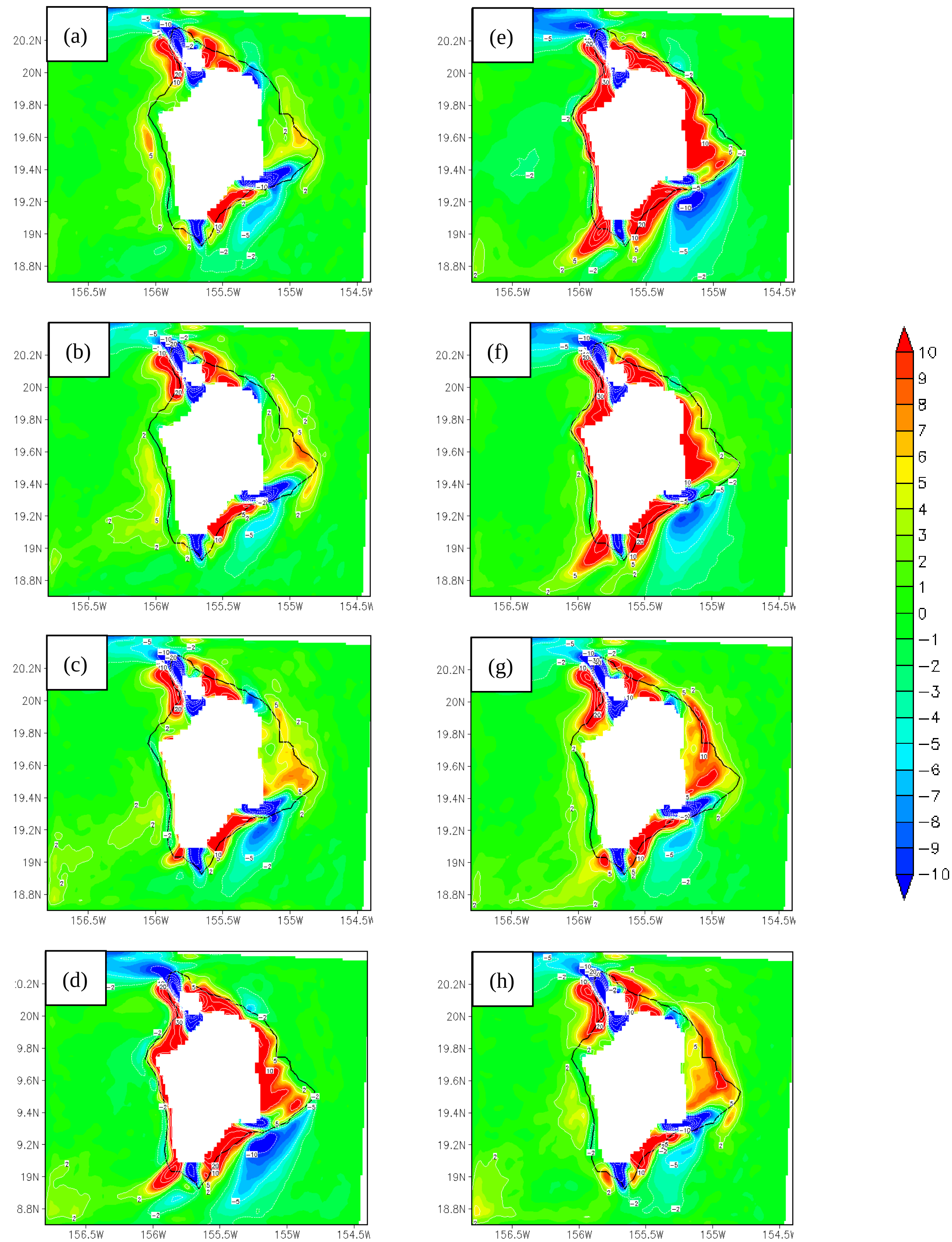

A 3 The simulated mean vertical motion (cm s^{-1}) over Hawai'i during the summer months at (a) 0200 HST, (b) 0500 HST, (c) 0800 HST, (d) 1100 HST, (e) 1400 HST, (f) 1700 HST, (g) 2000 HST, and (h) 2300 HST.

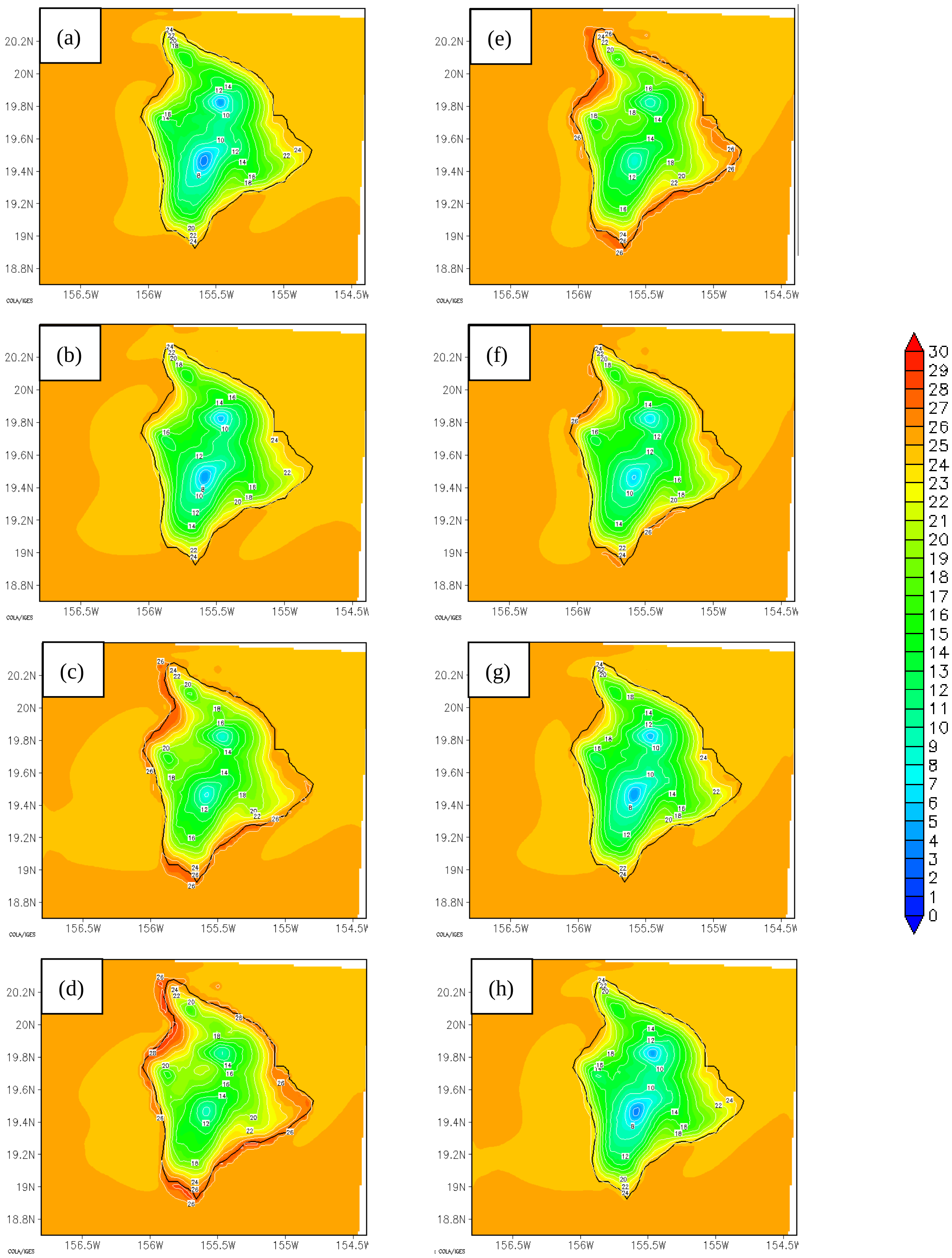

A 4 The simulated mean 2-m air temperature (℃) over Hawai'i during the summer months at (a) 0200 HST, (b) 0500 HST, (c) 0800 HST, (d) 1100 HST, (e) 1400 HST, (f) 1700 HST, (g) 2000 HST, and (h) 2300 HST.

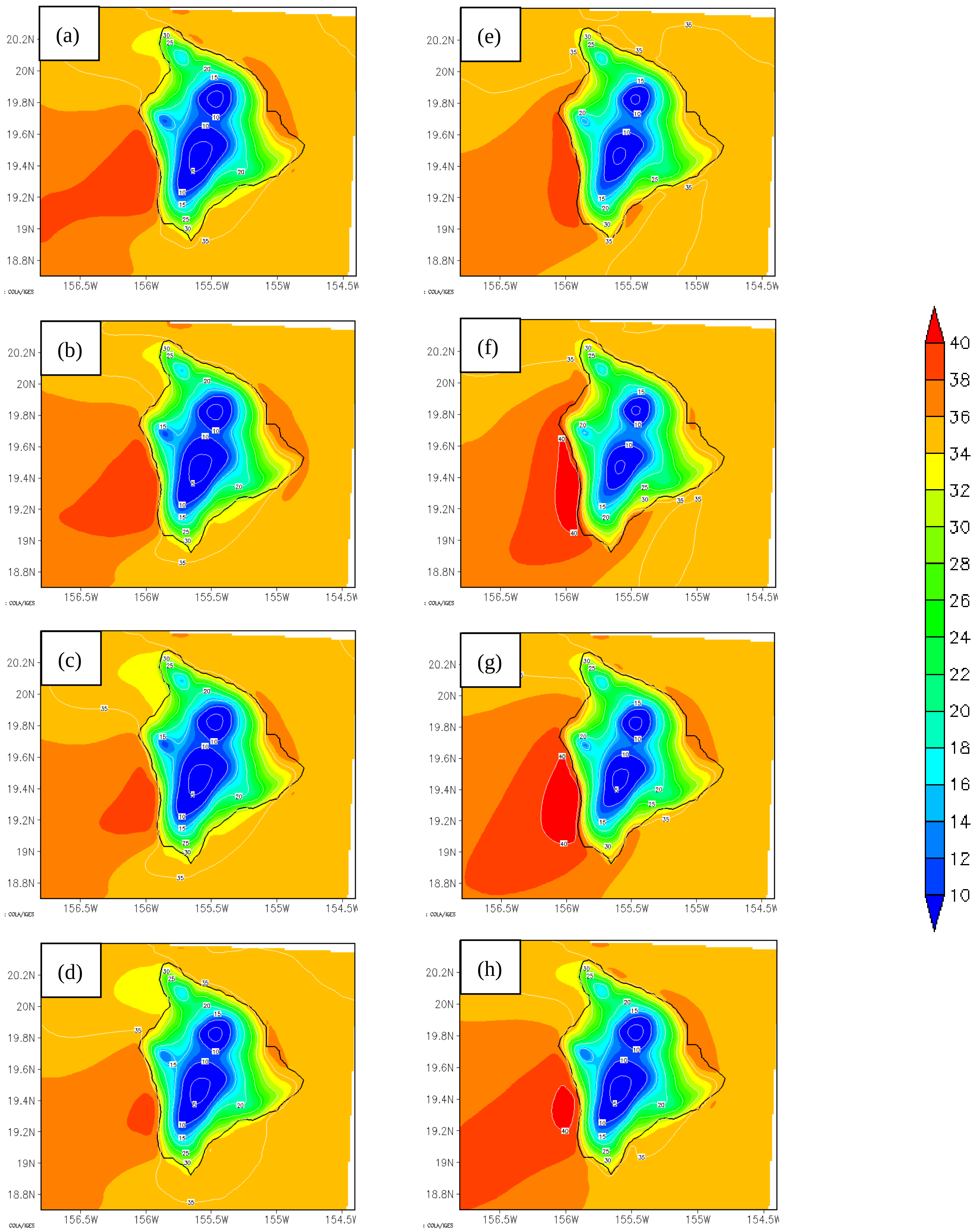

A 5 The simulated mean TPW (mm) over Hawai'i during the summer months at (a) 0200 HST, (b) 0500 HST, (c) 0800 HST, (d) 1100 HST, (e) 1400 HST, (f) 1700 HST, (g) 2000 HST, and (h) 2300 HST.

Appendix B: The Mean Diurnal Cycle with 3-hr Interval during the Winter Months

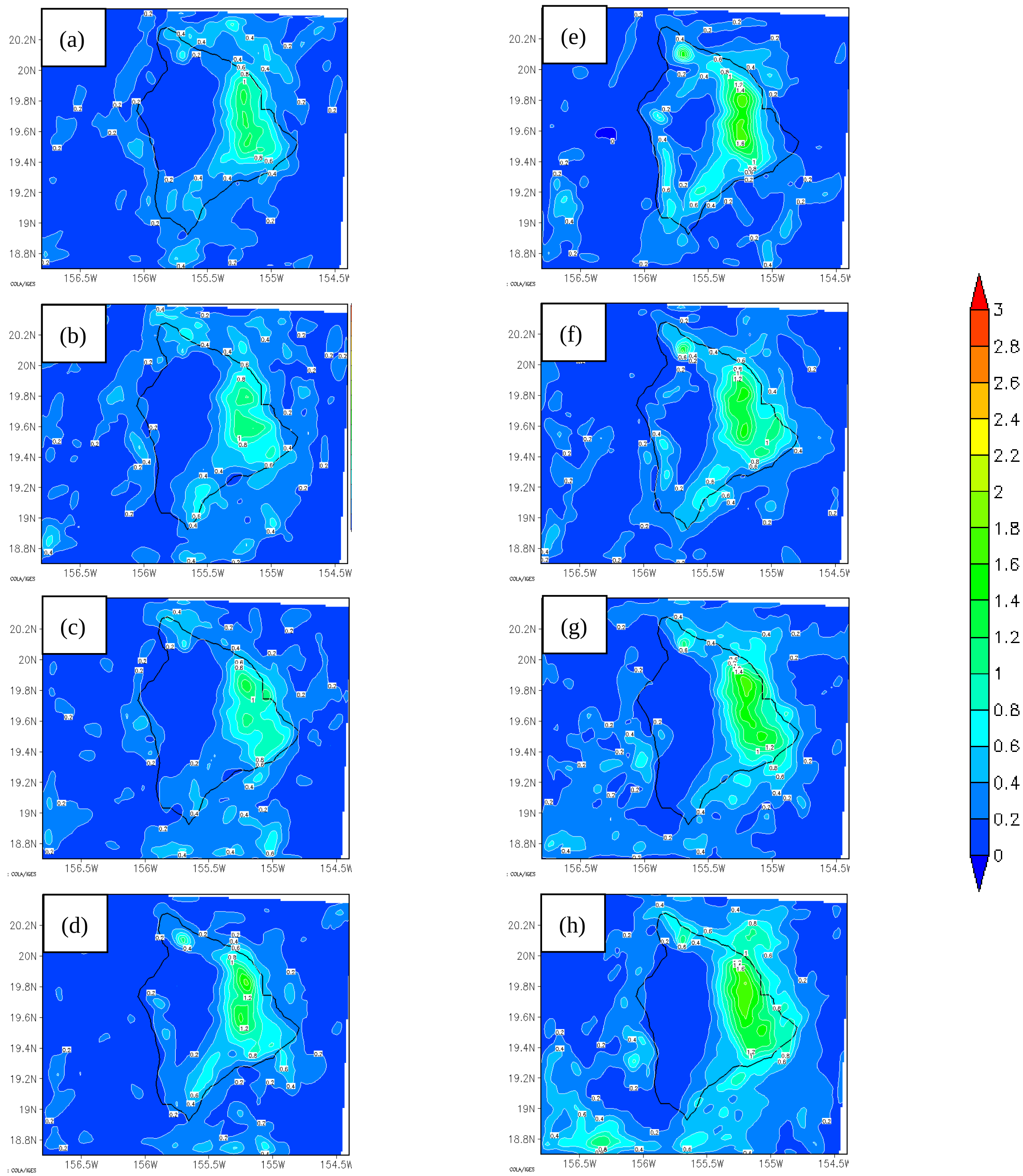

B 1 The simulated mean 3-h accumulated rainfall (mm) over Hawai'i during the winter months at (a) 1100-0200 HST, (b) 0200-0500 HST, (c) 0500-0800 HST, (d) 0800-1100 HST, (e) 1100-1400 HST, (f) 1400-1700 HST, (g) 1700-2000 HST, and (h) 2000-2300 HST.

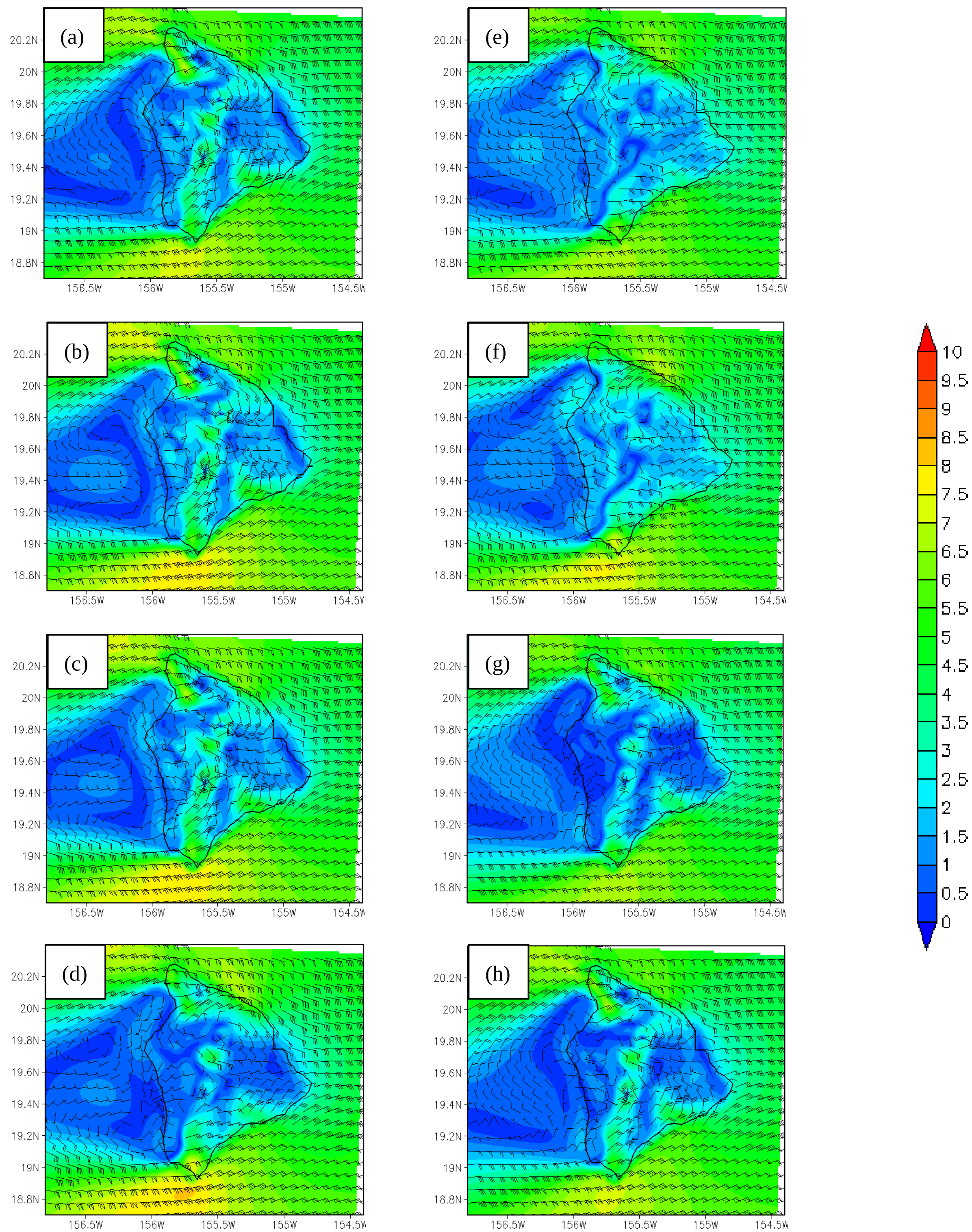

B 2 The simulated mean diurnal wind (m s^{-1}; full barb: 1 m s^{-1}, pennant: 5 m s^{-1}) over Hawai'i during the winter months at (a) 0200 HST, (b) 0500 HST, (c) 0800 HST, (d) 1100 HST, (e) 1400 HST, (f) 1700 HST, (g) 2000 HST, and (h) 2300 HST.

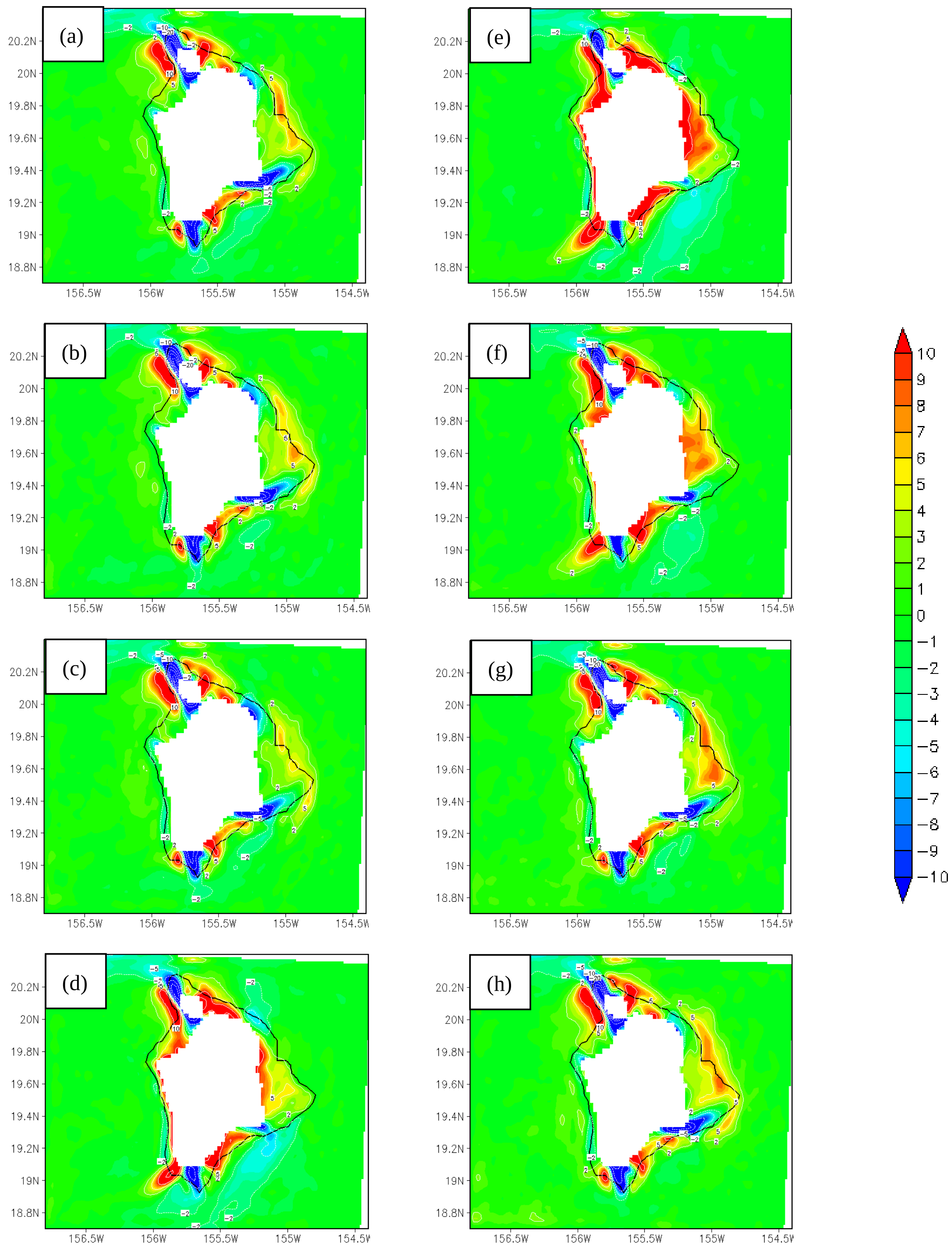

B 3 The simulated mean vertical motion (cm s^{-1}) over Hawai'i during the winter months at (a) 0200 HST, (b) 0500 HST, (c) 0800 HST, (d) 1100 HST, (e) 1400 HST, (f) 1700 HST, (g) 2000 HST, and (h) 2300 HST.

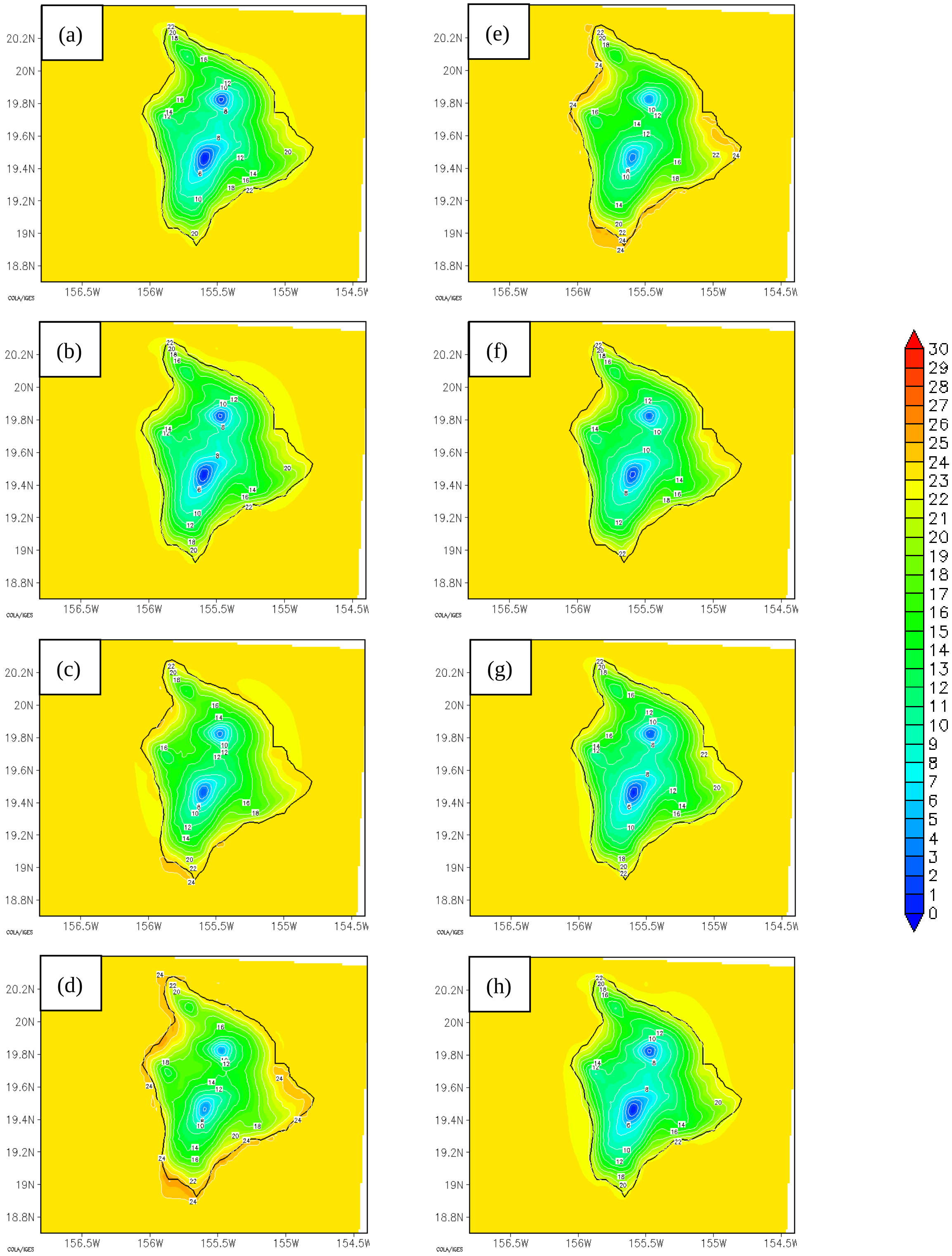

B 4 The simulated mean 2-m air temperature (℃) over Hawai'i during the winter months at (a) 0200 HST, (b) 0500 HST, (c) 0800 HST, (d) 1100 HST, (e) 1400 HST, (f) 1700 HST, (g) 2000 HST, and (h) 2300 HST.

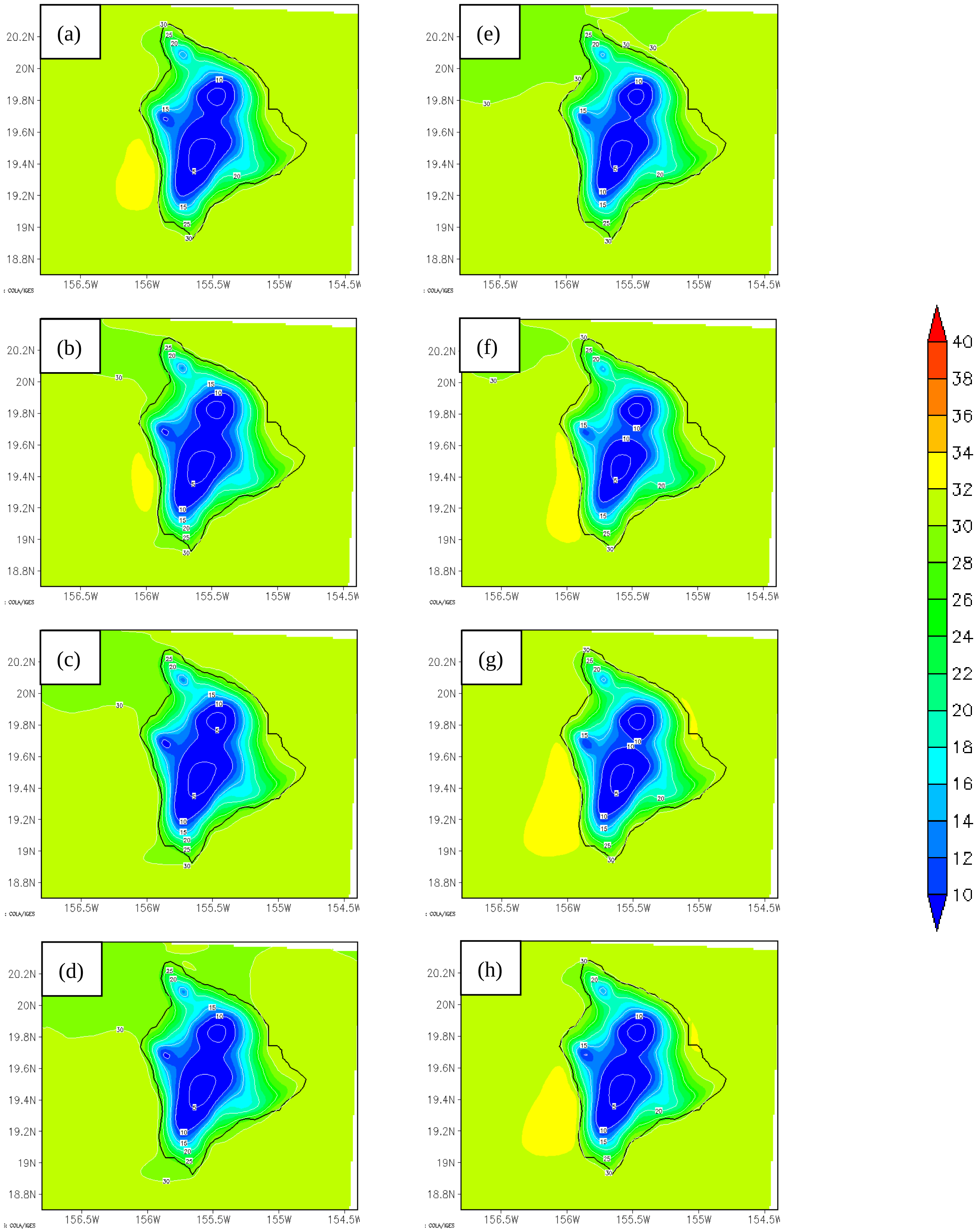

B 5 The simulated mean TPW (mm) over the island of Hawai'i during the winter months at (a) 0200 HST, (b) 0500 HST, (c) 0800 HST, (d) 1100 HST, (e) 1400 HST, (f) 1700 HST, (g) 2000 HST, and (h) 2300 HST.

Appendix C: The Mean Diurnal Cycle with 3-hr Interval under Winter Trade-wind Days

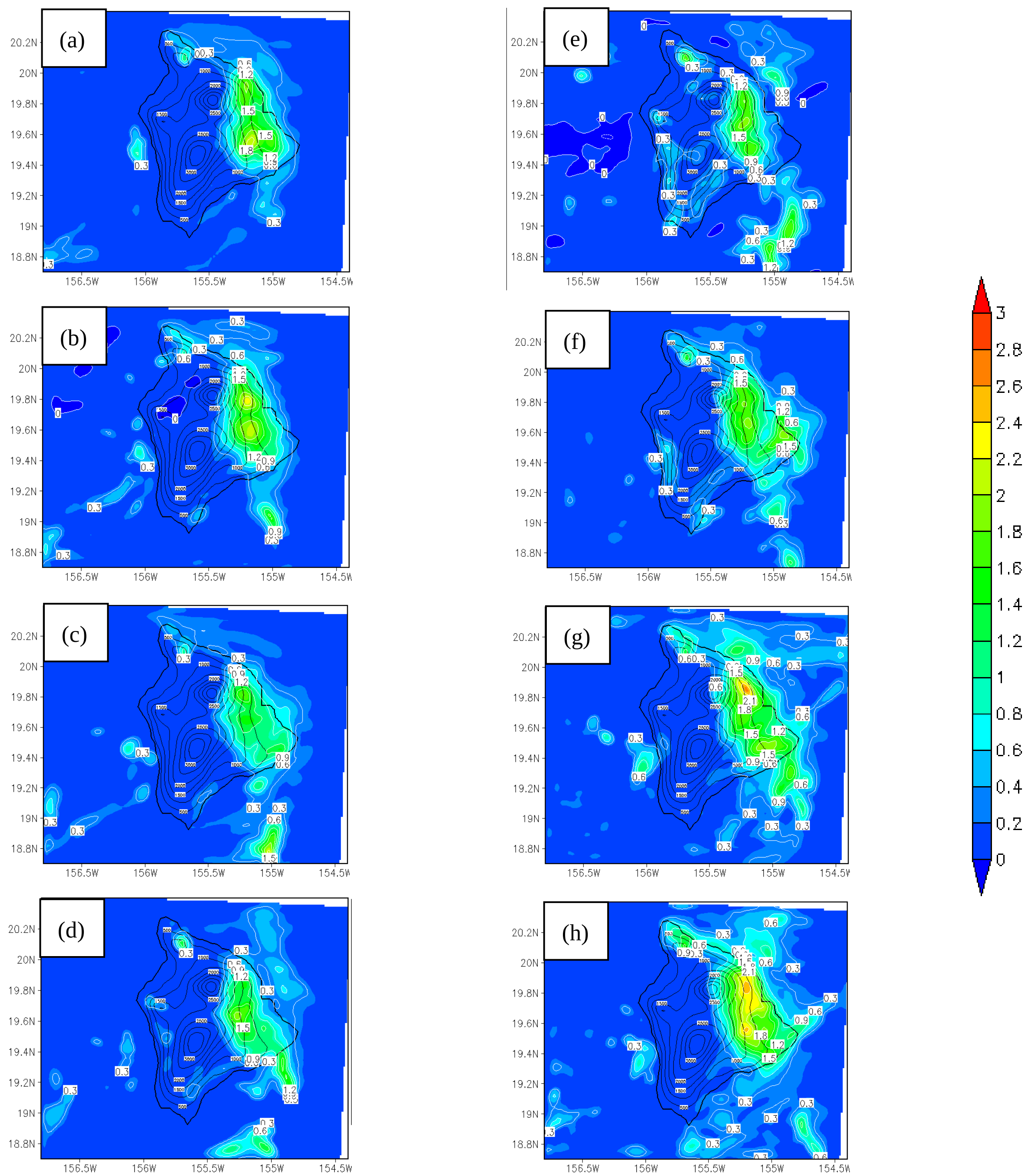

C 1 The simulated of the winter trade-wind days over Hawai'i: the mean 3-h accumulated rainfall (mm) and the altitude (m; black contour with CI = 500 m) at (a) 0200 HST, (b) 0500 HST, (c) 0800 HST, (d) 1100 HST, (e) 1400 HST, (f) 1700 HST, (g) 2000 HST, and (h) 2300 HST.

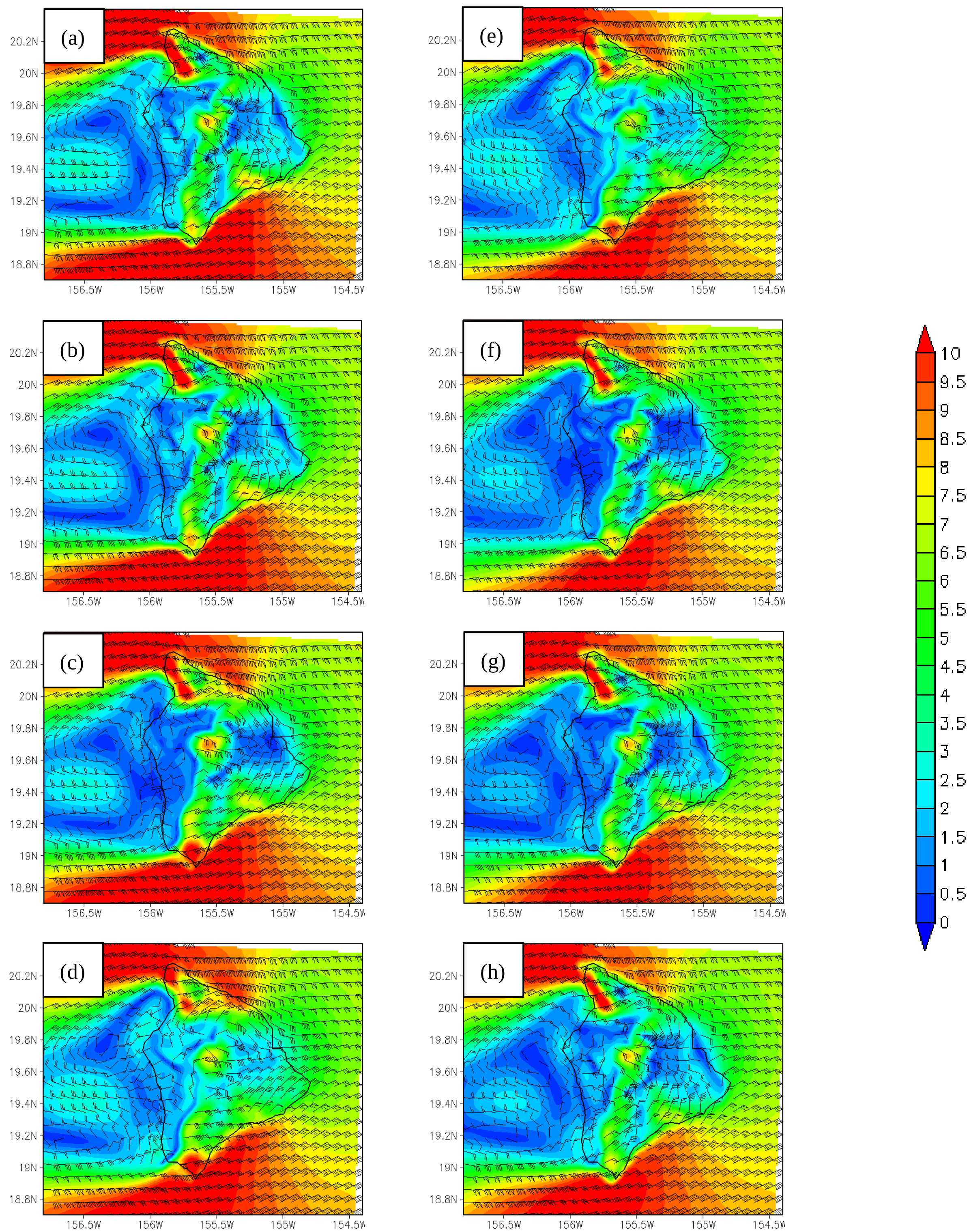

C 2 The simulated of the winter trade-wind days over Hawai'i: mean diurnal wind (m s^{-1}; full barb: 1 m s^{-1}, pennant: 5 m s^{-1}) at (a) 0200 HST, (b) 0500 HST, (c) 0800 HST, (d) 1100 HST, (e) 1400 HST, (f) 1700 HST, (g) 2000 HST, and (h) 2300 HST.

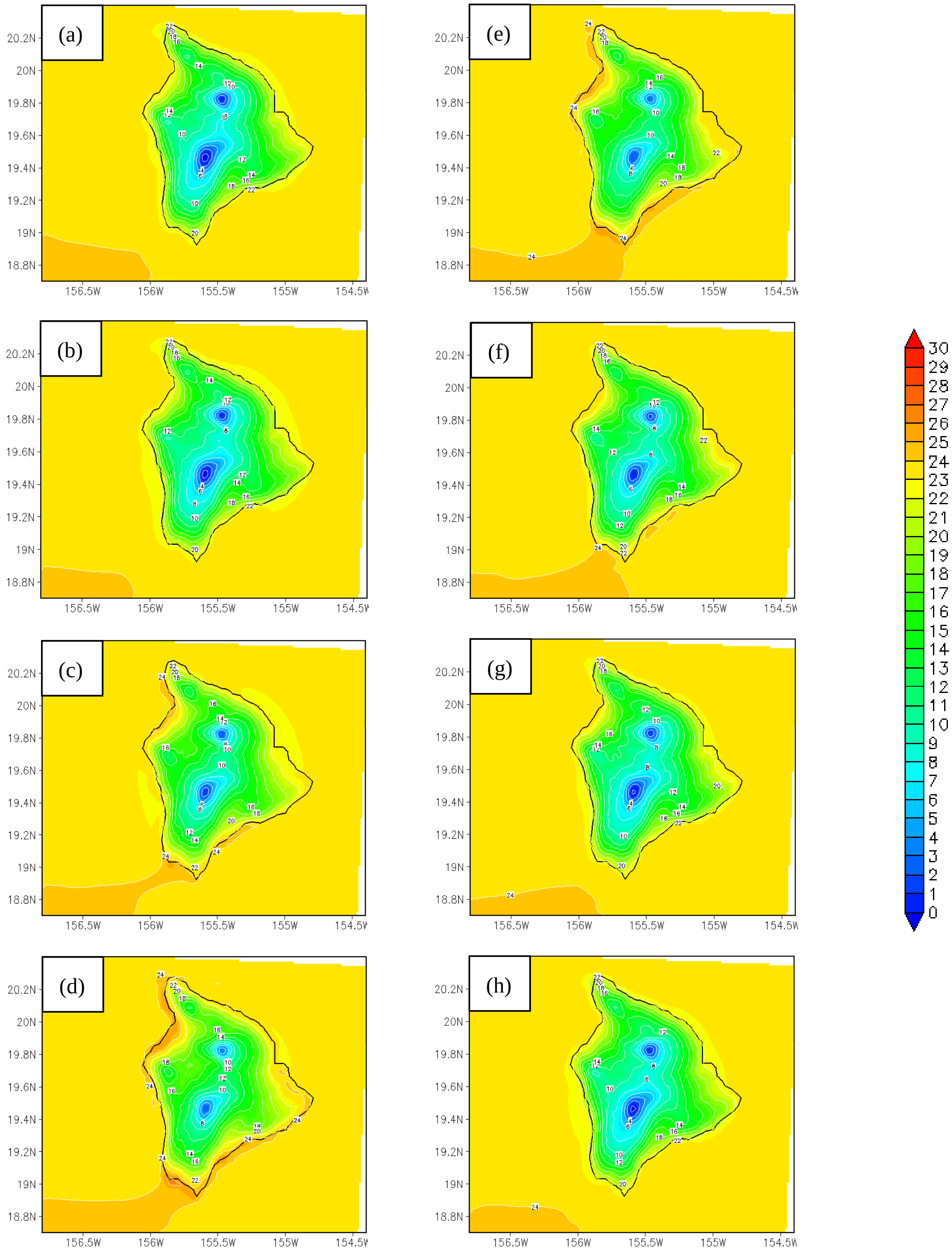

C 3 The simulated of the winter trade-wind days over Hawai'i: mean 2-m air temperature (℃) at (a) 0200 HST, (b) 0500 HST, (c) 0800 HST, (d) 1100 HST, (e) 1400 HST, (f) 1700 HST, (g) 2000 HST, and (h) 2300 HST.

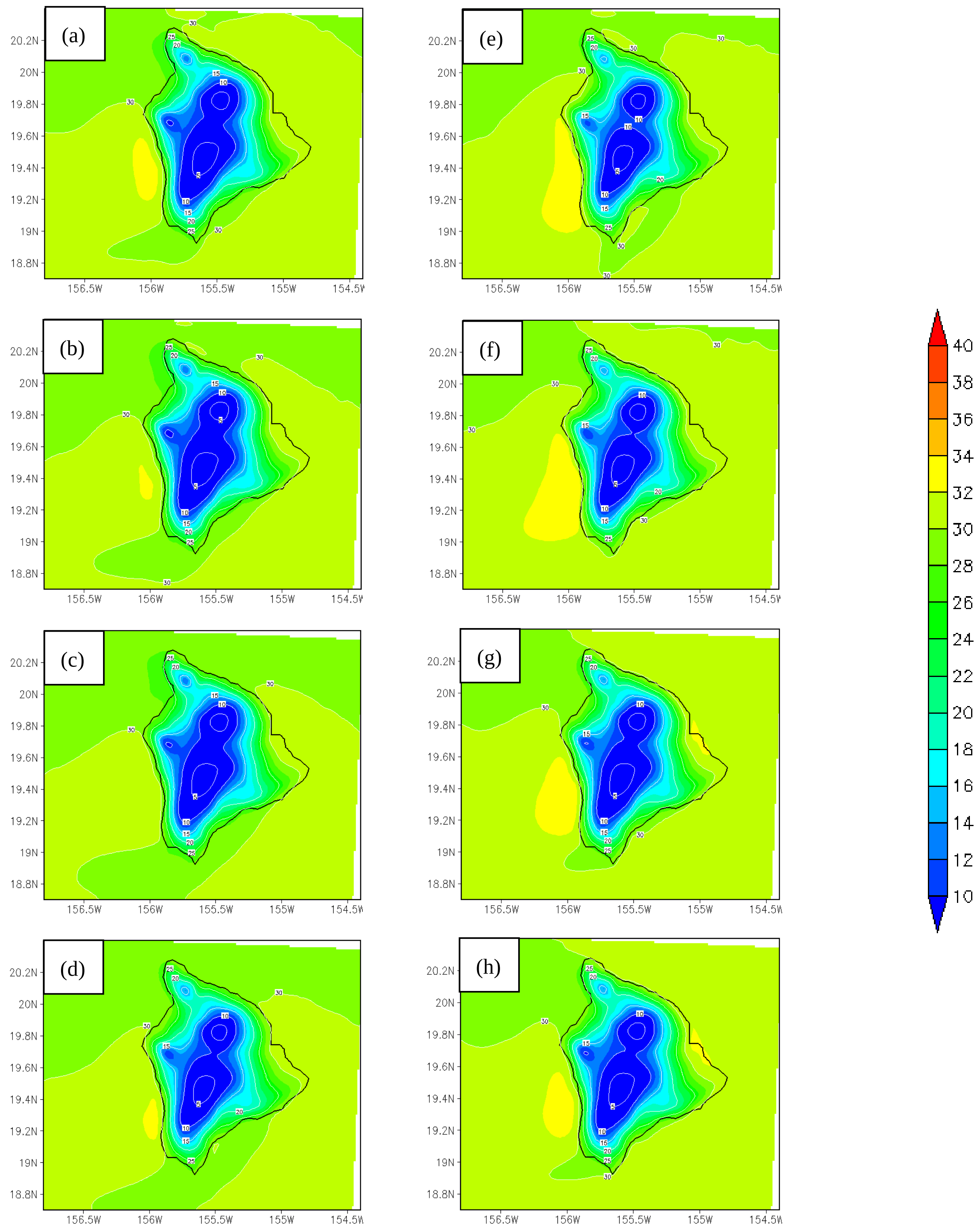

C 4 The simulated of the winter trade-wind days over Hawai'i: mean TPW (mm) at (a) 0200 HST, (b) 0500 HST, (c) 0800 HST, (d) 1100 HST, (e) 1400 HST, (f) 1700 HST, (g) 2000 HST, and (h) 2300 HST.

Appendix D: The Mean Diurnal Cycle with 3-hr Interval during the Summer Months

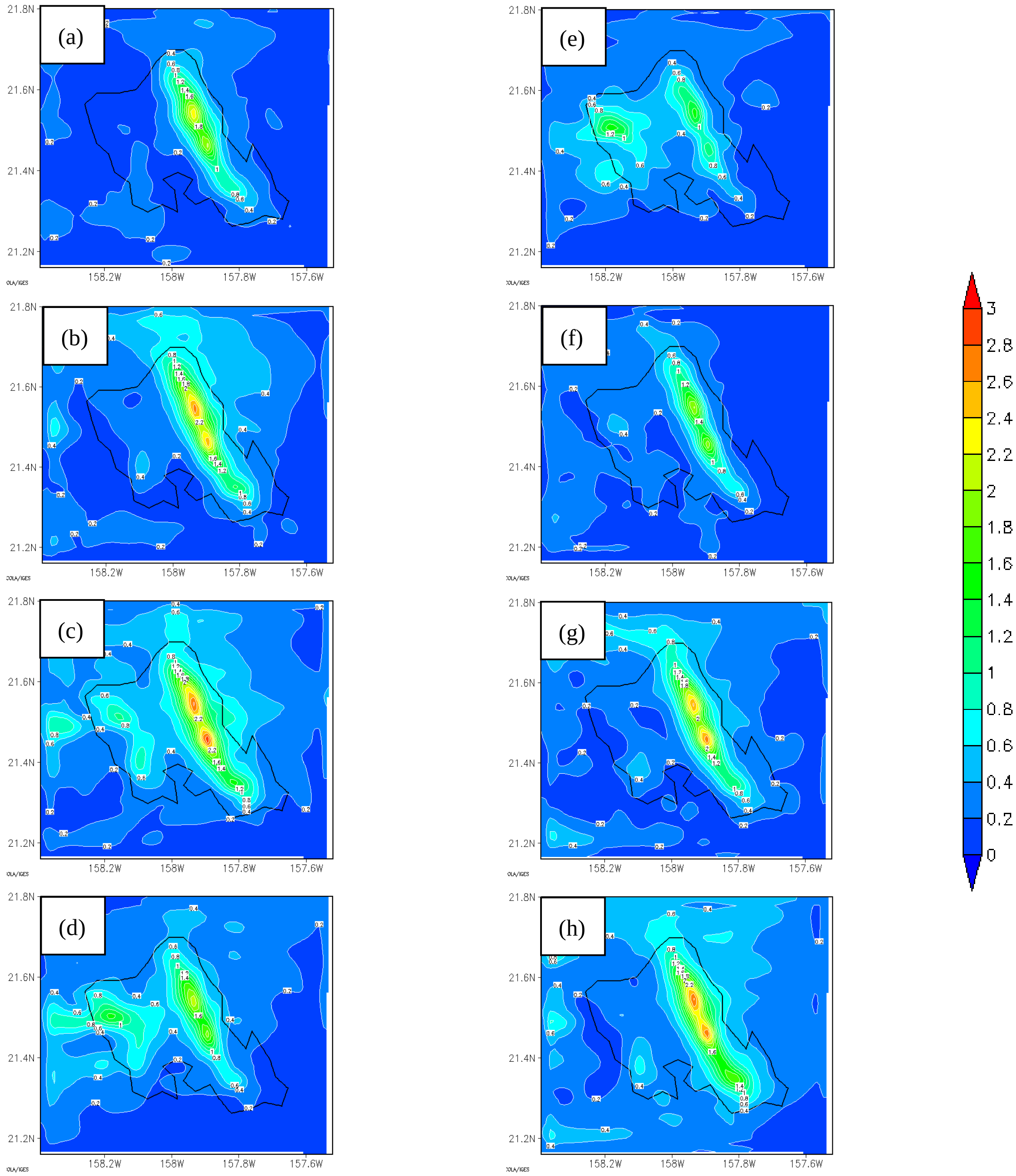

D 1 The mean 3-h accumulated rainfall (mm) over the Oahu during the summer months at (a) 0200 HST, (b) 0500 HST, (c) 0800 HST, (d) 1100 HST, (e) 1400 HST, (f) 1700 HST, (g) 2000 HST, and (h) 2300 HST.

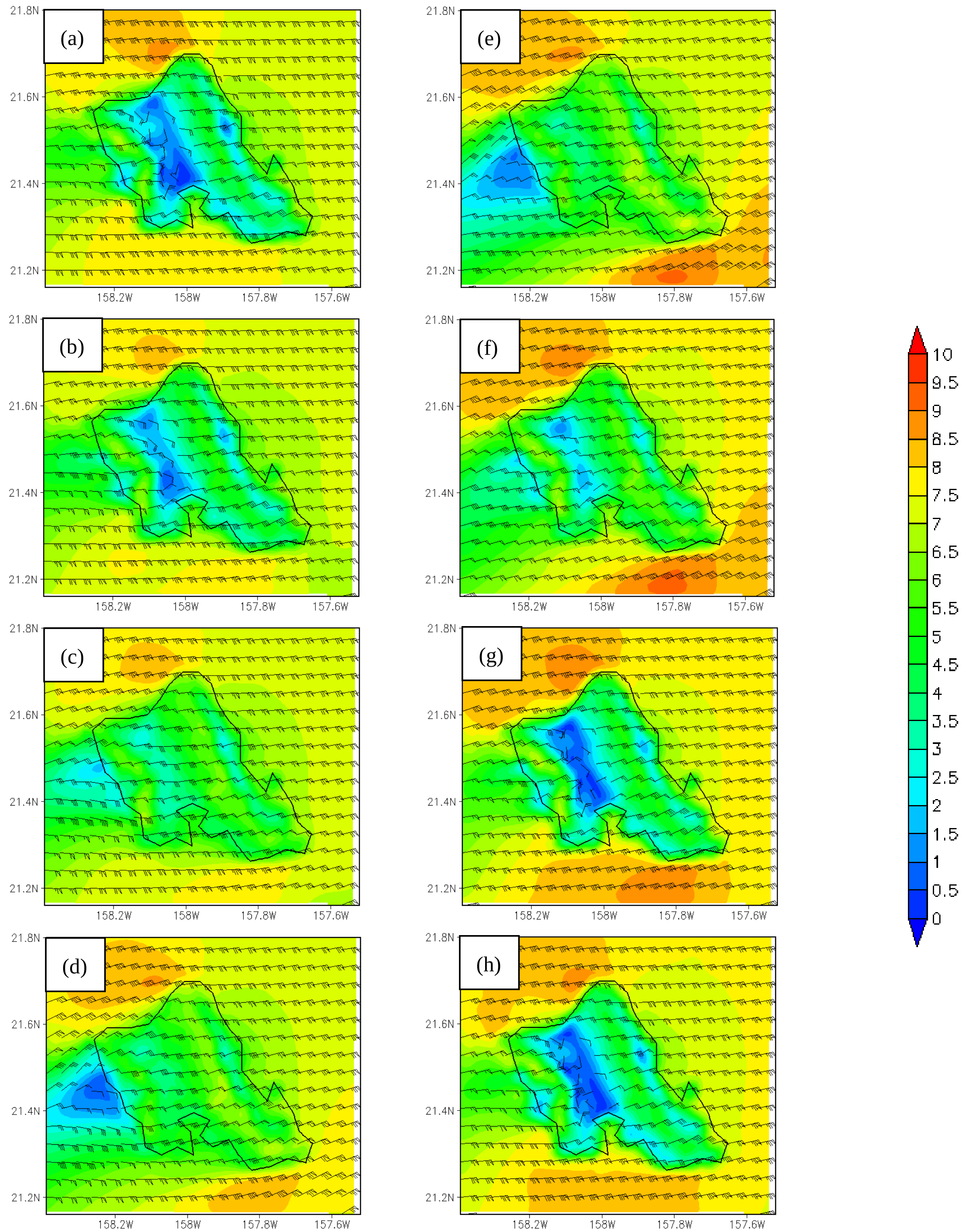

D 2 The simulated mean diurnal wind (m s^{-1}; full barb: 1 m s^{-1}, pennant: 5 m s^{-1}) over Oahu during the summer months at (a) 0200 HST, (b) 0500 HST, (c) 0800 HST, (d) 1100 HST, (e) 1400 HST, (f) 1700 HST, (g) 2000 HST, and (h) 2300 HST.

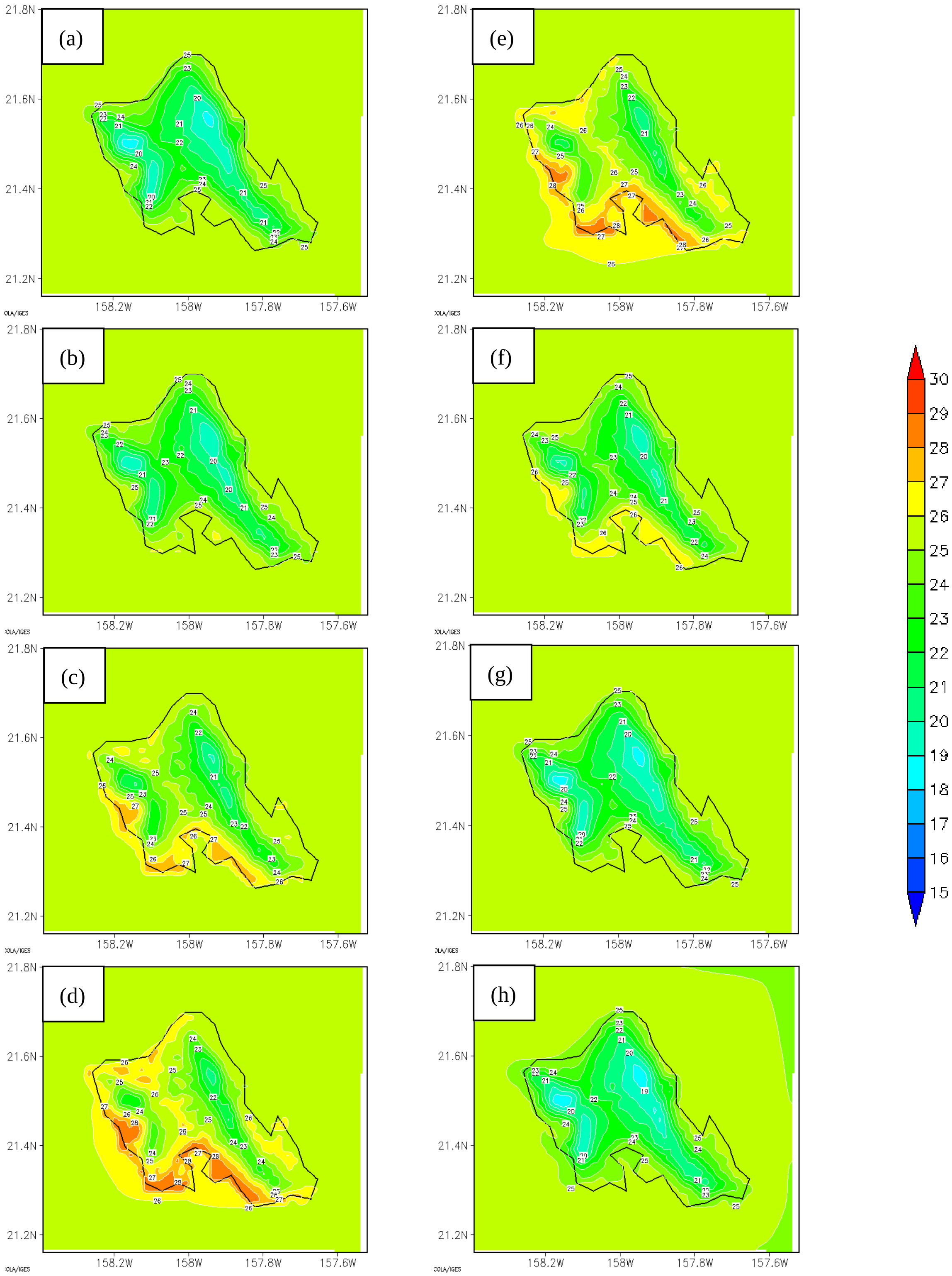

D 3 The simulated mean 2-m air temperature (℃) over Oahu during the summer months at (a) 0200 HST, (b) 0500 HST, (c) 0800 HST, (d) 1100 HST, (e) 1400 HST, (f) 1700 HST, (g) 2000 HST, and (h) 2300 HST.

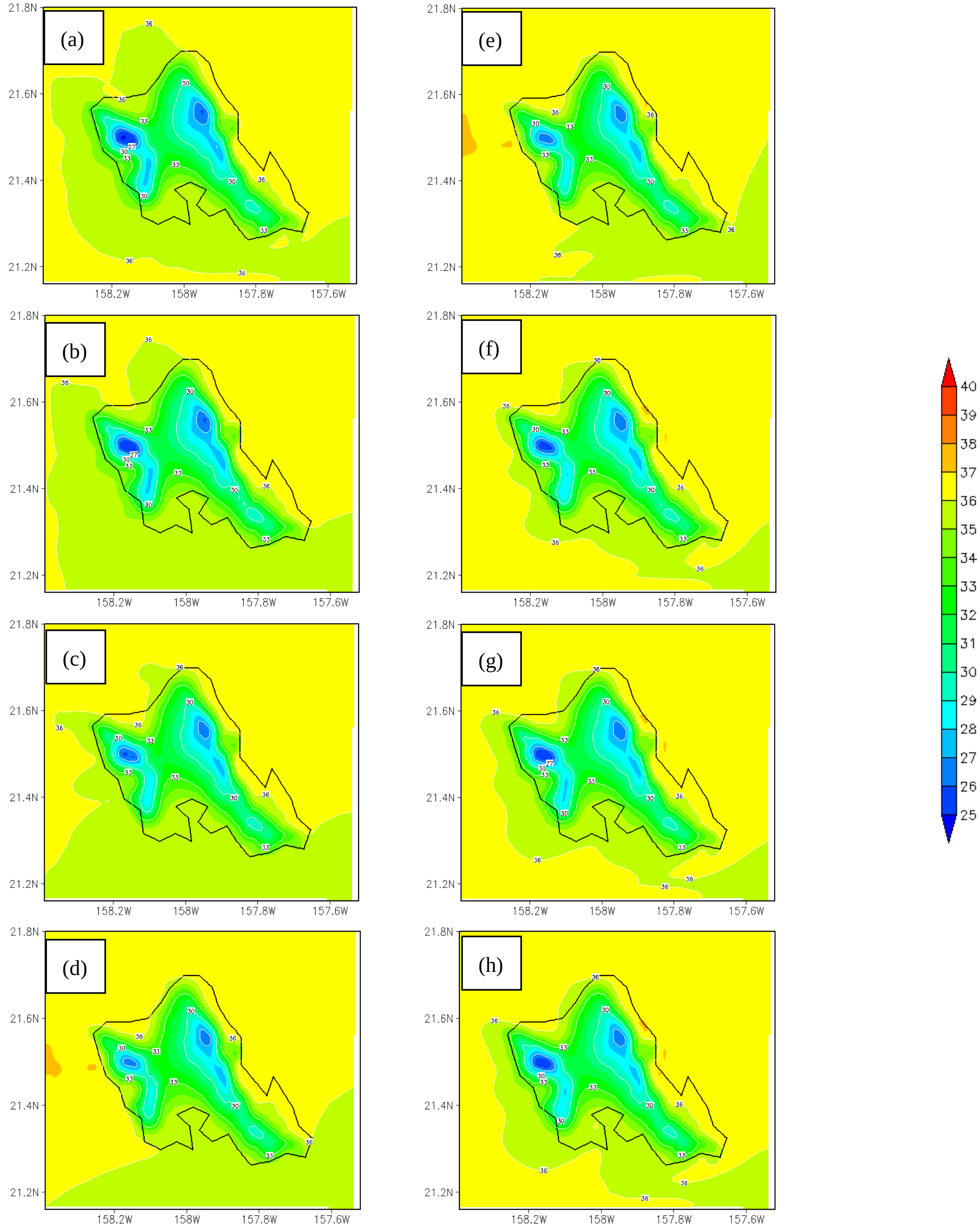

D 4 The simulated mean TPW (mm) over Oahu during the summer months at (a) 0200 HST, (b) 0500 HST, (c) 0800 HST, (d) 1100 HST, (e) 1400 HST, (f) 1700 HST, (g) 2000 HST, and (h) 2300 HST.

REFERENCES

Blumenstock, D.I. and Price, S. 1967. Climate of Hawai'i. In Climates of the States, no. 60-51, Climatography of the United States, U.S. Department of Commerce.

Carbone, R. E., J. D. Tuttle, W. A. Cooper, V. Grubišic´, and W. C. Lee, 1998: Trade wind rainfall near the windward coast of Hawai'i. *Mon. Wea. Rev.,* **126,** 2847–2863.

Carlis, D., L., Y.-L. Chen, and V. Morris, 2010: Numerical simulations of island-scale airflow and the Maui vortex during summer trade-wind conditions. Mon. Wea. Rev. **138**, 2706-2736.

Chen, F. and J. Dudhia, 2001: Coupling an Advanced Land Surface–Hydrology Model with the Penn State–NCAR MM5 Modeling System. Part I: Model Implementation and Sensitivity. *Mon. Wea. Rev.*, **129**, 569–585.

Chen, Y.-L., and A. J. Nash, 1994: Diurnal variation of surface airflow and rainfall frequencies on the Island of Hawai'i. *Mon. Wea. Rev.*, **122**, 34-56.

——, and J. Feng, 1995: The Influences of Inversion Height on Precipitation and Airflow over the Island of Hawai'i. *Mon. Wea. Rev.*, **123**, 1660–1676.

Dudhia, J., 1989: Numerical study of convection observed during the Winter Monsoon Experiment using a mesoscale twodimensional model. *J. Atmos. Sci.*, **46**, 3077–3107.

Feng, J., and Y.-L. Chen, 1998: Evolution of katabatic winds on the Island of Hawai'i during 10 August 1990. *Mon. Wea. Rev.*, **126**, 2185-2199.

Garrett, A. J., 1980: Orographic cloud over the eastern slopes of Mauna Loa Volcano, Hawai'i, related to insolation and wind. *Mon. Wea. Rev.*, **108,** 931–941.

Giambelluca, T. W., M. A. Nullet, and T. A. Schroeder, 1986: Rainfall Atlas of Hawai'i. Rep. R76, Dept. of Land and Natural Resources, Honolulu, HI, 267 pp.

Grell, G. A., 1993: Prognostic evaluation of assumptions used by cumulus parameterizations. *Mon. Wea. Rev.*, **121**, 764–787.

Hong, S.-Y., and H. L. Pan, 1996: Nonlocal boundary layer vertical diffusion in a medium-range forecast model. *Mon. Wea. Rev.*, **124**, 2322–2339.

Hsie, E.-Y., R. A. Anthes, and D. Keyser, 1984: Numerical simulation of frontogenesis in a moist atmosphere. *J. Atmos. Sci.*, **41**, 2581–2594.

Lyons, S. W., 1982: Empirical Orthogonal Function Analysis of Hawai'ian Rainfall. *J. Appl. Meteor.*, **21**, 1713–1729.

Leopold, L. B., 1948: Diurnal weather patterns on Oahu and Lanai, Hawai'i. *Pac. Sci*., 2, 81–95.

Leopold, L. B., 1949: The interaction of trade wind and sea breeze, Hawai'i. *J. Meteor.*, **6**, 312–320.

Loveridge, E. H., 1924: Diurnal variations of precipitation at Honolulu, Hawai'i. *Mon. Wea. Rev.,* **52**, 584–585.

Meisner, B. N. 1976: *A study of Hawai'ian and Line Islands rainfall*. Honolulu: Dept. Meteorology, University of Hawai'i (U.H. Met. 76-04).

Nguyen, H. V., Y.-L. Chen, and F. Fujioka, 2010: Numerical Simulations of island effects on airflow and weather during the summer over Oahu. *Mon. Wea. Rev.* **138**, 2253–2280.

Nickerson, E. C., and M. A. Dias, 1981: On the existence of atmospheric vortices downwind of Hawai'i during the HAMEC project. *J. Appl. Meteor.,* **20,** 868–873.

Patzert, W. C., 1969: Eddies in Hawai'ian waters. Hawai'i Institute of Geophysics Rep. HIG-69-8, University of Hawai'i, 51 pp.

Schär, C. and R. B. Smith, 1993: Shallow-Water Flow past Isolated Topography. Part II: Transition to Vortex Shedding. *J. Atmos. Sci.*, **50**, 1401–1412.

Schroeder, T., 1981: Characteristics of local winds in northwest Hawai'i. *J. Appl. Meteor.,* **20,** 874–881.

——, 1993: Climate controls. Prevailing Trade Winds, M. Sanderson, Ed., University of Hawai'i Press, 12–36.

Schroeder, T., B. J. Kilonsky, and B. N. Meisner, 1977: Diurnal variation in rainfall and cloudiness. UHMET Rep. 77-03, Dept. of Meteorology, University of Hawai'i, Honolulu, HI, 67 pp.

Smith, R. B., 1989: Hydrostatic flow over mountains. Advances in Geophysics, Vol. 31, Academic Press, 1–41.

——, and V. Grubišic´, 1993: Aerial observation of Hawai'i's wake. *J. Atmos. Sci.*, **50,** 3728–3750.

Smolarkiewicz, P. K., and R. Rotunno, 1989: Low Froude number flow past three-dimensional obstacles. Part I: Baroclinically generated lee vortices. *J. Atmos. Sci.*, **46,** 1154–1164.

——, R. M. Rasmussen, and T. L. Clark, 1988: On the dynamics of Hawai'ian cloud bands: Island forcing. *J. Atmos. Sci.*, **45,** 1872–1905.

Takahashi, T., 1977: Rainfall at Hilo, Hawai'i. *J. Meteor. Soc. Japan*, **55,** 121–129.

Wang, J.-J., and Y.-L. Chen, 1998: A case study of Hawai'ian trade wind rainbands and their interaction with the island-induced airflow. *Mon. Wea. Rev.*,**126**, 409-423.

Yang, Y., and Y.-L. Chen, 2003: Circulations and rainfall on the leeside of the Island of Hawai'i during HaRP. *Mon. Wea. Rev.*, **131**, 2525–2542.

——, ——, and F. M. Fujioka, 2005: Numerical simulations of the island-induced circulation over the Island of Hawai'i during HaRP. *Mon. Wea. Rev.* **133**, 3693-3713.

——, and ——, 2008: Effects of terrain heights and sizes on island-scale circulations and rainfall for the Island of Hawai'i during HaRP. *Mon. Wea. Rev.* **136**, 120-146.

——, ——, and F. M. Fujioka, 2008: Effects of trade wind strength and direction on the leeside circulations and rainfall of the Island of Hawai'i. *Mon. Wea. Rev.* **136**, 4799-4818.

Yang, Y., S. -P. Xie, and J. Hafner, 2008: The Thermal Wake of Kauai Island: Satellite Observations and Numerical Simulations*. *J. Climate*,**21**, 4568–4586.

Zhang,Y.,Y.-L. Chen, S.-Y. Hong,H.-M. H. Juang, and K. Kodama, 2005a: Validation of the coupled NCEP mesoscale spectral model and an advanced land surface model over the Hawai'ian Islands. Part I: Summer trade-wind conditions and a heavy rainfall event. *Wea. Forecasting*, **20**, 847–872.

Zhang, Y., Y.-L. Chen, and K. Kodama, 2005b: Validation of the Coupled NCEP Mesoscale Spectral Model and an Advanced Land Surface Model over the Hawai'ian Islands. Part II: A High Wind Event*. *Wea. Forecasting*, **20**, 873–895.